

Self-Supervised Learning for Image Segmentation: A Comprehensive Survey

Thangarajah Akilan[†], *Senior Member, IEEE*, Nusrat Jahan[†], *Graduate Student Member, IEEE*,
Wandong Zhang, *Member, IEEE*

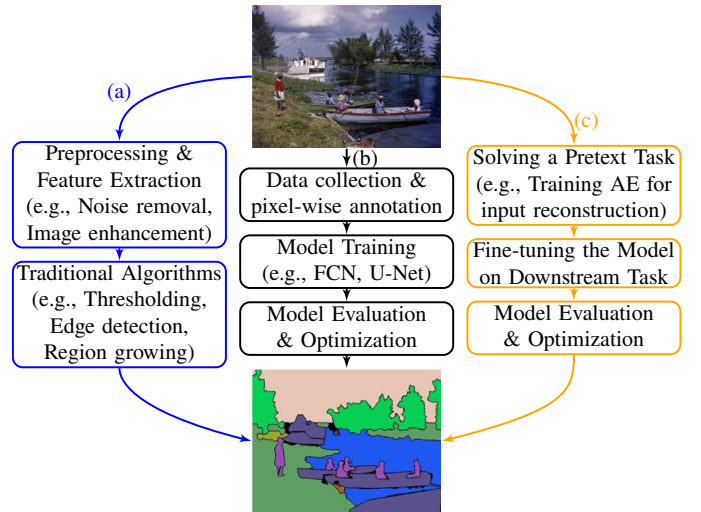
Abstract—Supervised learning demands large amounts of precisely annotated data to achieve promising results. Such data curation is labor-intensive and imposes significant overhead regarding time and costs. Self-supervised learning (SSL) partially overcomes these limitations by exploiting vast amounts of unlabeled data and creating surrogate (pretext or proxy) tasks to learn useful representations without manual labeling. As a result, SSL has become a powerful machine learning (ML) paradigm for solving several practical downstream computer vision problems, such as classification, detection, and segmentation. Image segmentation is the cornerstone of many high-level visual perception applications, including medical imaging, intelligent transportation, agriculture, and surveillance. Although there is substantial research potential for developing advanced algorithms for SSL-based semantic segmentation, a comprehensive study of existing methodologies is essential to trace advances and guide emerging researchers. This survey thoroughly investigates over 150 recent image segmentation articles, particularly focusing on SSL. It provides a practical categorization of pretext tasks, downstream tasks, and commonly used benchmark datasets for image segmentation research. It concludes with key observations distilled from a large body of literature and offers future directions to make this research field more accessible and comprehensible for readers.

Index Terms—Image segmentation, machine learning, representation learning, self-supervised learning.

I. INTRODUCTION

IMAGE segmentation is a pixel-level classification process that partitions an input image into multiple segments that are more meaningful for high-level applications. For instance, segmentation generates foreground masks that delineate objects while suppressing background details, offering a more information-rich representation than simple bounding boxes. Such masks are particularly beneficial for applications like video surveillance. Over the past few decades, various segmentation techniques have been developed in three main learning paradigms: traditional methods, end-to-end supervised deep learning (DL), and self-supervised learning, as illustrated in Fig. 1. Traditional approaches, including intensity thresholding, histogram-based clustering, edge detection, region growing, graph cuts, probabilistic models, conditional random fields [1], [2], etc., rely on predefined heuristics, hypotheses, and preset hyperparameters rather than explicit training and model evaluation. These methods extract salient features from preprocessed input images before performing segmentation and can yield reliable results in controlled environments. However, their performance often deteriorates in real-world scenarios, where variations in input data are unpredictable.

[†]contributed equally to this work.



The pipelines (a), (b), and (c), represent traditional, supervised, and SSL approaches used for image segmentation, respectively. Note: In (a), there is no explicit model evaluation since there is no training involved unlike in (b) or (c). The input and output images are adopted from [13].

Fig. 1: Three widely used image segmentation techniques.

Recent advancements in DL, have significantly enhanced image segmentation through end-to-end training on large-scale labeled datasets. DL architectures originally developed for image classification, have been effectively adapted for segmentation employing fully convolutional networks (FCNs), upsampling, transposed convolution (ConvT), and residual feature concatenation [3]. These innovations have gained state-of-the-art (SOTA) performance in medical image segmentation [4], moving object segmentation, and semantic segmentation [5]–[7]. Concurrently, semi-supervised and weakly-supervised learning approaches have received the attention of the computer vision community [8]–[12] due to their ability to reduce dependence on labeled data. This shift has driven a transition from traditional supervised learning to SSL.

A. The Paradigm Shift from Supervised Learning to SSL

SSL is a rapidly advancing field as it can learn latent features from unlabeled data. It employs pretext tasks, where pseudo-labels are generated directly from raw data, enabling model training without manual annotation. Once pre-trained, the model can be fine-tuned with minimal labeled data on a target domain [14]–[16]. This process closely mirrors human learning, where knowledge is acquired incrementally through feedback and adaptation. In contrast, supervised learning heav-

TABLE I: A comparative summary of existing surveys on self-supervised-driven techniques for visual data analysis.

Ref.	Objective	Targeted Application	Contribution
[30] 2021	Categorization of pretext tasks	■, □, ☒	Covering general SSL pipelines, terminologies, deep neural networks, evaluation metrics, and datasets used for visual feature learning.
[31] 2021	Comparative analysis on both supervised and SSL approaches	□, ☒	Highlighting recent works in SSL using contrastive learning and clustering methods, and listing of open challenges.
[32] 2021	Exploring SSL methods in the field of medical image analysis	Medical image analysis	Categorizing the SSL techniques in medical image analysis, and comparing their performances on benchmark datasets.
[33] 2021	Reviewing the SOTA methods in SSL for computer vision	General computer vision & medical image analysis	A high-level overview of the state-of-the-art SSL methods in computer vision tasks and medical image analysis; grouping them as predictive, generative, and contrastive self-supervised methods.
[34] 2022	A comprehensive overview of SSL using contrastive learning and auxiliary pretext	■, □, ☒	Organizing various SSL techniques and examining recent research in this field; conducting performance analyses of different SSL approaches.
[3] 2022	Survey on DL-based image segmentation techniques	■	Exploring a wide range of cutting-edge semantic, and instance-level segmentation methods; investigating commonly used datasets.
[15] 2024	Survey on SSL methods, covering their basics and application domains	Broad area of CV and NLP	Focused on visual SSL in four groups: context-based, contrastive learning, generative, and contrastive generative algorithms.
This Survey	Image segmentation-focussed a concise yet detailed investigation of SSL	■	A comprehensive overview of SSL approaches; an intuitive categorization of SSL-based image segmentation models with their application examples; a curated review of benchmark datasets; a depth analysis of SSL challenges in image segmentation and emerging research directions.

Note: ■ - Segmentation, □ - Object detection, ☒ - Classification, and SSL - self-supervised learning.

ily depends on large annotated datasets, which are costly and time-intensive to create, particularly in complex domains such as medical image analysis. Moreover, supervised models are prone to generalization errors, spurious correlations, and adversarial attacks. SSL mitigates these issues by leveraging unlabeled data to capture intrinsic patterns, reducing dependence on annotations, and improving domain adaptation. As a result, SSL has gained significant traction across various applications, including image classification [17]–[19], object recognition [20]–[23], image segmentation [24]–[27], and NLP applications, like emotion recognition [28], [29].

B. Existing Survey

Table I summarizes existing key surveys, highlighting their objectives and contributions. Chen *et al.* [35] review supervised DL methods for cardiac image segmentation, while Minaee *et al.* [3] examine DL image segmentation models, analyzing their interconnections, strengths, and challenges. Liu *et al.* [36] explore DL approaches for brain tumor segmentation, discussing architectures, performance under imbalanced data, and multi-modality strategies.

However, few surveys focus on SSL, where most of them address SSL in classification [30], object detection [37], image recognition [31], and remote sensing [38]. Xu [32] provides a concise overview of SSL frameworks, evaluating their performance on benchmark medical image datasets. Some studies examine SSL’s domain adaptation for downstream applications. Rani *et al.* [39] summarize such downstream tasks and relevant datasets. Hao *et al.* [5] group semantic segmentation models based on supervision levels, while Shurrab and Duwairi [33] survey SSL methods for medical imaging without analyzing model performance. Jing and Tian [30] classify SSL pretext tasks into four types and compare their performances. Despite extensive research on image segmentation, most surveys emphasize supervised algorithms. Studies dedicated to self-supervised segmentation remain limited, underscoring the need for this work to bridge the gap.

The rest of this article is structured as follows: Section II lays a foundation of SSL. Section III systematically reviews the SSL methods used for image segmentation. Section IV lists benchmark datasets. Section V discusses the challenges and directions for the prospect of SSL. Finally, Section VI concludes the article.

C. Contributions

Given SSL’s effectiveness in addressing data scarcity, this article presents an in-depth comparative analysis of recent SSL-based segmentation algorithms. The key contributions of this study are: (i) A comprehensive review of self-supervised learning approaches, (ii) A systematic categorization of SSL-based image segmentation models and their applications, (iii) A curated review of benchmark datasets for training and evaluation, (iv) An analysis of SSL challenges in image segmentation and emerging research directions.

II. PRELIMINARY

A. Self-supervised Learning

Fig. 2 on page 3 illustrates the general workflow of SSL-driven model building. It involves (i) defining pretext label-free task, (ii) data preparation for the pretext task, (iii) representation learning via self-supervision, (iv) knowledge transfer, (v) fine-tuning on downstream task, and (vi) performance rating.

1) *Pretext Task*: It serves as the cornerstone of SSL, enabling self-supervision without the need for manually annotated labels. The core idea is to start with simpler pretext tasks and progressively refine the model for more complex downstream tasks. Various pretext tasks, viz. jigsaw puzzles [42], rotation prediction [43], context encoding [44], [45], sequence prediction [46]–[48], and image denoising [49], [50]—are designed to extract domain-specific features [34], [51]. These tasks facilitate learning generalized representations from raw data, which are then exploited for downstream applications. Pretext and downstream tasks often share semantic overlap,

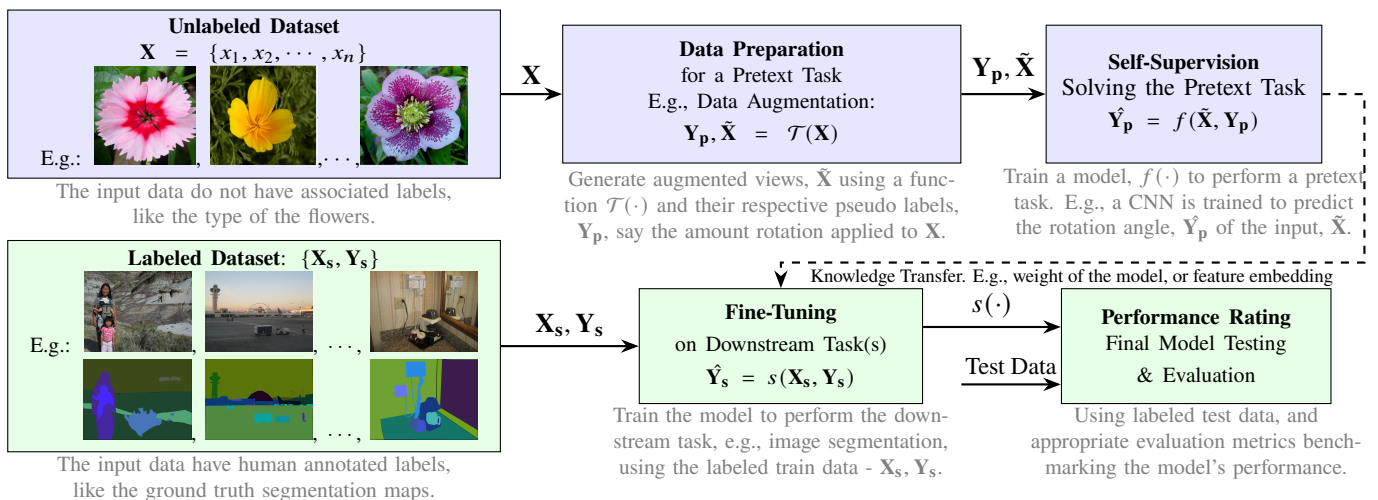


Fig. 2: SSL-driven model development. (a) data preparation - $\mathcal{T}(\cdot)$ create synthetic samples $\tilde{\mathbf{X}}$ with pseudo labels \mathbf{Y}_p from the unlabeled data \mathbf{X} (b) self-supervised training - a model is trained using $\{\tilde{\mathbf{X}}, \mathbf{Y}_p\}$, (c) fine-tuning - the model is fine-tuned on a downstream task using a labeled dataset $\{\mathbf{X}_s, \mathbf{Y}_s\}$, and (d) performance rating - the final model is evaluated using test data of the target application. The unlabeled and labeled samples are adopted, respectively from [40] and [41].

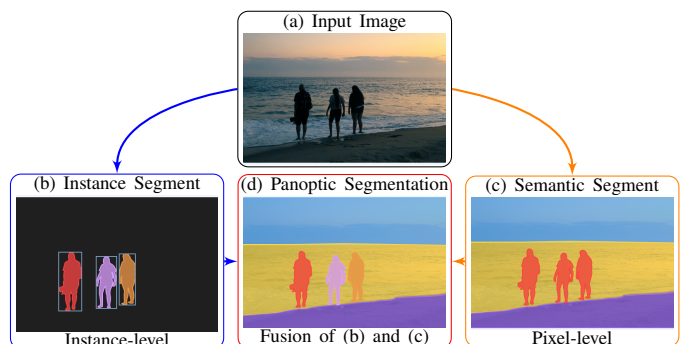
allowing multiple pretext tasks to be combined for robust feature learning [52], [53]. However, designing an effective pretext task requires careful formulation: (i) **balancing complexity**—tasks that are too simple may fail to capture meaningful features, while overly complex tasks risk overfitting or learning irrelevant patterns; (ii) **domain alignment**—ensuring the pretext task is structured to prevent shortcut learning and effectively transfer knowledge to the downstream objective.

2) *Representation Learning via Self-supervision*: It involves extracting useful, generalizable features from raw data, as the model optimizes an objective function while solving a pretext task. Each pretext task is tailored to the input data type and target application, leading to variations in the objective function. The goal is to guide models to learn meaningful representations using synthetically generated inputs from the unlabeled data, $\tilde{\mathbf{X}}$, and their pseudo-labels, \mathbf{Y}_p . A generic objective function is defined as the average loss over N samples in a mini-batch:

$$\mathcal{L} = \frac{1}{N} \sum_{n=1}^N J(\tilde{X}^n, Y_p^n), \quad (1)$$

where \tilde{X}^n and Y_p^n are the n th input sample and its pseudo-label, respectively, and $J(\cdot)$ computes the per-sample loss (the difference between the predicted label \hat{Y}_p and pseudo-label Y_p). The effectiveness of SSL hinges on the quality of the representations that encode essential input features, thereby improving generalization across diverse downstream tasks.

3) *Fine-tuning on Downstream Task*: A downstream task is the model's intended application [12], [54]. In this phase, the pre-trained representation learning model is adapted using labeled data of the target domain, with fine-tuning involving partial or full retraining and integration of a task-specific top layer. During fine-tuning, the target task-specific objective functions and evaluation metrics are applied to optimize and assess model performance.



The input and output images are adopted from <https://www.v7labs.com>.

Fig. 3: For a given (a) Input, (b) instance segmentation: per-object mask and class label, (c) semantic segmentation, and (d) panoptic segmentation: per-pixel class + instance-level labels.

B. Image Segmentation

Image segmentation assigns pixel-level labels to partition an image into sub-regions, serving as a key pillar for detailed scene understanding and various applications. Segmentation approaches fall into three main categories as illustrated in Fig. 3: instance segmentation [55]–[57], semantic segmentation [58]–[60], and panoptic segmentation [61]–[63], which unifies the first two. Among these, semantic segmentation has seen widespread adoption in domains, viz. agriculture, healthcare, infrastructure management, and transportation [64].

For example, in healthcare, deep convolutional neural networks (DCNNs) are used for tasks, like tumor segmentation from brain MRIs [65], [66] and whole-heart segmentation from computed tomography (CT) images [67]. Similarly, precision agriculture relies on segmentation for insect detection, leaf disease identification, flower and crop recognition, farmland anomaly analysis, etc. However, applying deep supervised learning to image segmentation still faces 4 major challenges: (i) handling high-resolution inputs, (ii) accommodating diverse

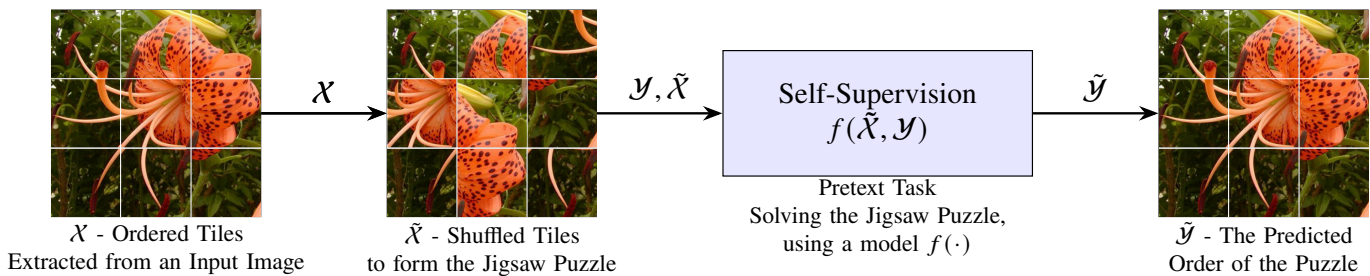


Fig. 4: Illustration of the Jigsaw puzzle. An input image is divided into tiles (\mathcal{X}) and then shuffled ($\tilde{\mathcal{X}}$), where \mathcal{Y} is the pseudo label denoting the correct order of the tiles. The model is trained to rearrange the shuffled tiles to the correct order.

object shapes and sizes, (iii) requiring large-scale, densely annotated datasets, and (iv) achieving accurate delineation of segmentation boundaries [67]–[70]. Recent works address these challenges using label-efficient SSL [71]–[74].

III. PRETEXT TASK FOR IMAGE SEGMENTATION

To perform image segmentation, various types of pretext tasks are employed in SSL. These pretext tasks can be broadly categorized into three groups based on the nature of the learning objective: predictive methods, generative methods, and contrastive methods [8], [30], [75]–[77].

A. Predictive Methods

Predictive methods generate pseudo-labels by applying transformations or masking strategies to infer specific properties of the input data. Common predictive pretext tasks include slice order prediction, jigsaw puzzles, Rubik’s cube problems, and rotation prediction. However, the effectiveness of these tasks varies, as their utility depends on their alignment with the underlying objectives of the segmentation task.

1) *Jigsaw puzzle*: Jigsaw puzzle-solving is a classical pattern recognition problem involving the reassembly of disordered visual fragments, first addressed by Freeman and Garder in 1964 [42]. In self-supervised image segmentation, it serves as a pretext task to train a model, $f(\cdot)$, to learn spatial relationships between image patches, as shown in Fig. 4. It involves partitioning an image into patches, shuffling them, and training the model to recover the original arrangement. By solving this spatial reasoning problem, the model learns useful representations for downstream tasks.

Noroozi and Favaro [78] introduced this approach by extracting nine non-overlapping 80×80 patches from an image, labeling each by its original position, and training a model to predict the correct order when given a shuffled sequence. The trained model functions as a feature extractor (backbone), with a downstream task-specific sub-network fine-tuned on the target dataset. Yang *et al.* [79] extended this method by increasing the number of patches to 25, introducing slight overlaps, and enlarging the patch size to 115×115 . These modifications improved semantic segmentation performance by capturing finer low-level features, such as edge and texture continuity, essential for precise segmentation. Beyond natural image segmentation tasks, the jigsaw puzzle has also been used in medical image analysis. For example, Taleb *et al.* [80]

applied this for CT scan and MRI image segmentation tasks. They considered the puzzle as a self-supervised reconstruction problem, in which a model is trained by minimizing the reconstruction error between the sorted ground truth patch sequence, P^* , and the reconstructed version of the shuffled input patch sequence, P as in (2).

$$\mathcal{L}_{\text{puzzle}}(\theta, P, P^*) = \sum_{i=1}^K \|P_i^* - S_{\theta, P_i}^T \cdot P_i\|^2, \quad (2)$$

where θ and K stand for the model parameters, and the total number of training puzzles, respectively. Hence, $S_{\theta, P_i}^T \cdot P_i$ is the reconstructed version of the i -th puzzle. Through training, the model would capture different tissue structures that were important for the downstream task. Thus, Taleb *et al.* fine-tuned the model in various target domains for segmentation (prostate segmentation, brain tumor segmentation, liver segmentation) and regression problems (patient survival days prediction).

Building on earlier works, this puzzle-solving has been further explored as a pretext task for image segmentation [81], clustering [82], video anomaly detection [83], medical image classification [84], and out-of-distribution detection [85]. Advanced variants, such as 3D jigsaw and spatiotemporal jigsaw, introduce additional complexity, enabling models to learn more robust spatial, temporal, and geometric relationships, thus improving downstream performance [32], [86]. However, this approach has key **limitations**: model performance is highly sensitive to puzzle tile size and permutation complexity, and it incurs substantial computational costs.

2) *Slice Order Prediction*: Ordering, a basic concept in mathematics and combinatorial optimization, predates modern computing. Early mechanical devices, such as Babbage’s analytical engine [87], laid the groundwork for contemporary sorting algorithms. In computer vision, ordering is framed as a sequential verification task, akin to the jigsaw puzzle [88]–[92], but primarily applied to volumetric data (e.g., MRI, CT, PET). It captures the inherent 3D structure by learning spatial relationships between 2D slices. As illustrated in Fig. 5 on page 5, the task is formulated as: (i) **pretext data generation**—sampling a data volume or video into 2D frames, generating correctly ordered (\mathcal{S}_{\checkmark}) and incorrectly ordered (\mathcal{S}_{\times}) sequences; and (ii) **self-supervised training**—training a model, $\Phi(\cdot)$, to maximize probability p of correctly ordered tuples. Alternatively, some studies formulate this as a reconstruction problem [47], [92]–[94]. Formally, given a set of images, $\mathcal{I} \in \mathbb{R}^{C \times H \times W}$, the model reconstruct an attribute

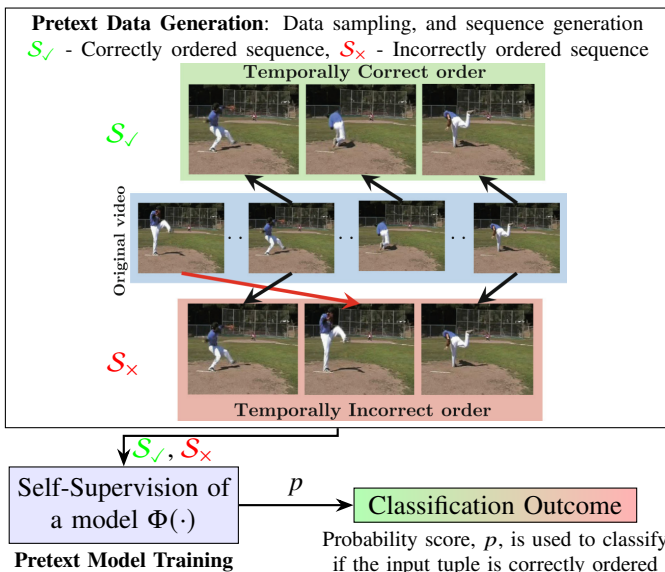


Fig. 5: Illustration of slice order prediction pretext task. The image inside the block is adopted from [89].

map, $\mathbf{S}_{\text{rec}} \in \mathbb{R}^{F \times H \times W}$ and sequence order $\mathbf{y}_{\text{order}} \in \mathbb{Z}^F$: $y_{\text{order},i} \in \{0, 1, 2, \dots, F-1\}$ as in (3).

$$\mathbf{S}_{\text{rec}} = \Phi(\mathcal{I}_0, \mathcal{I}_1, \dots, \mathcal{I}_{F-1}), \quad (3)$$

where the model Φ is trained to order an arbitrary sequence of F images shuffled from a volumetric data or temporal sequence. For example, in [47], a multi-task representation learning strategy is introduced with two pretext tasks aimed at predicting (i) the next slice and (ii) the previous slice in a sequence from a randomly selected slice of a volumetric CT scans. This strategy helps the model learn to map from x_i^j to x_i^{j-t} and x_i^{j+t} , capturing the structural similarity, including the relative location, shape, size, and structure of the organs. The model is optimized using the standard Euclidean distance defined by (4), which serves as the objective function.

$$\mathcal{L}_{\text{pretext}} = \sum_i \left(\|f_{\theta}^{-}(x_i^j) - x_i^{j-t}\| + \|f_{\theta}^{+}(x_i^j) - x_i^{j+t}\| \right), \quad (4)$$

where $f_{\theta}^{-}(\cdot)$, and $f_{\theta}^{+}(\cdot)$ represent the models, in this case, decoder sub-networks that perform the backward sequence prediction and forward sequence prediction, respectively. While, x_i^j , x_i^{j-t} and x_i^{j+t} , denote the j th, $(j-t)$ th, and $(j+t)$ th slices, respectively, in the i th CT scan. Similarly, Spitzer *et al.* [95] developed slice ordering as a geodesic distance prediction task along the brain surface, to learn spatial relationships between adjacent slices in 3D medical images. This task can be extended to anomaly detection, where frame sequences are shuffled, and the model predicts the correct temporal order or reconstructs the original video [89], [92], [96].

3) *Rotation Prediction*: In this task, a geometric transformation, specifically rotation, is applied to the input image, and a model is trained to predict the applied transformation through classification or regression [43]. Prior research has demonstrated that rotation prediction can be an effective self-supervised pretext task for downstream applications, such as

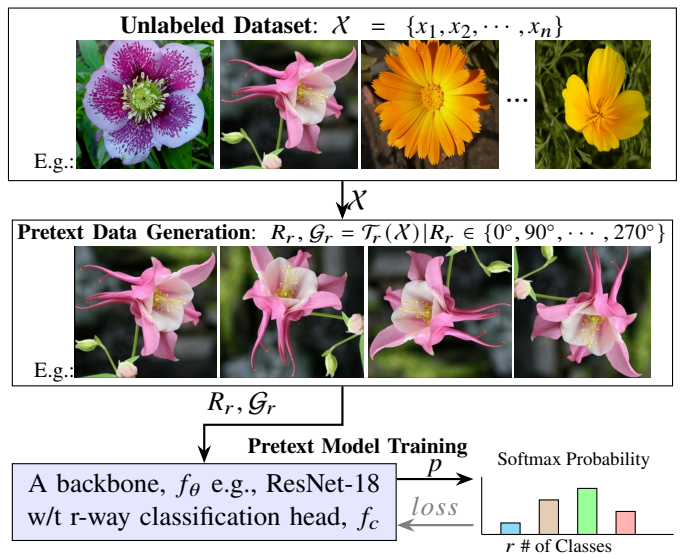


Fig. 6: Overview of the rotation prediction pretext task.

object detection, recognition, and segmentation. For instance, [97] and [98] employ a transformation function $\mathcal{T}_r(\cdot)$, which rotates an input image x_1 by an angle R_r randomly chosen from a predefined set $\{0^\circ, 90^\circ, 180^\circ, 270^\circ\}$, generating the transformed sample \mathcal{G}_r , as illustrated in Fig. 6. A model $f_{\theta}(\cdot)$, parameterized by θ , is then trained to predict the rotation angle using a classification head f_c by minimizing the cross-entropy loss (\mathcal{L}_{CE}) between the true one-hot encoded label R_r and the predicted probability distribution $f_c(f_{\theta}(\mathcal{G}_r))$:

$$\mathcal{L}_{\text{rot}} = \frac{1}{4} \sum_{r \in \{0^\circ, 90^\circ, 180^\circ, 270^\circ\}} \mathcal{L}_{\text{CE}}(R_r, f_c(f_{\theta}(\mathcal{G}_r))), \quad (5)$$

where \mathcal{L}_{rot} denotes the mean classification loss over four rotations, and $f_c(\cdot)$ outputs a Softmax probability distribution over rotation classes.

In addition to conventional classification tasks, [98] explores co-training self-supervised rotation prediction alongside supervised tasks, assessing its impact on robustness and generalization under distribution shifts. Their findings indicate that self-supervised pretext tasks can improve model resilience in challenging environments. Meanwhile, [97] mitigates rotation ambiguity by designing a nonparametric similarity-based approach that distinguishes instance-specific and rotation-invariant features, yielding superior performance across classification, detection, and segmentation tasks. Additionally, Linmans *et al.* [99] integrate rotation-equivariant CNN architectures with rotation prediction pre-training to improve tumor segmentation.

Despite its advantages, rotation prediction exhibits certain **limitations**. Its effectiveness varies across architectures and tasks, as the pre-learned features may not generalize optimally. Moreover, the reliance on discrete rotation angles limits the model's ability to capture continuous transformations, potentially making learned representations overly task-specific and less adaptable to real-world variations.

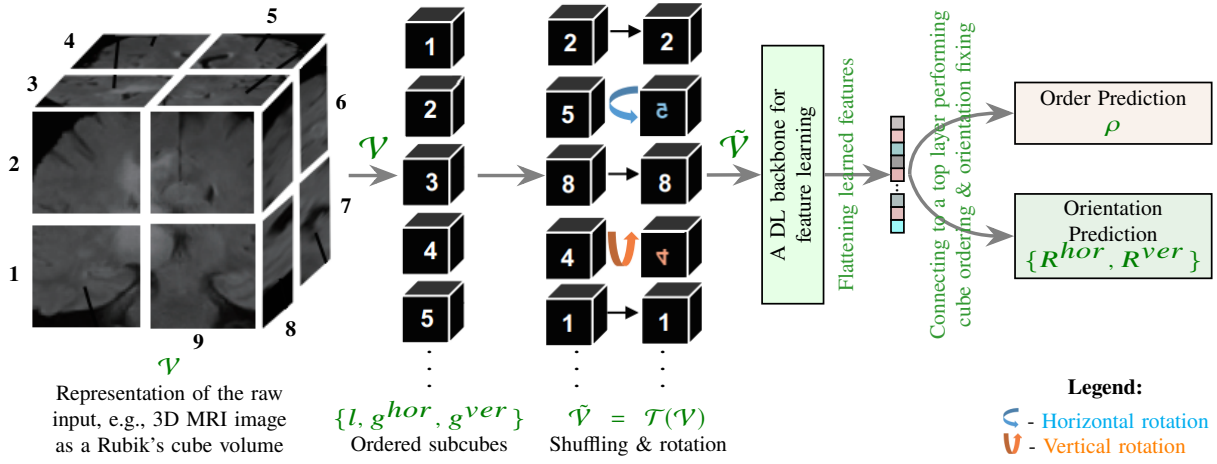


Fig. 7: Illustration of the Rubik's cube recovery-like pretext task. The input is divided into subcubes and a problem is formulated by cube shuffling, then a model is trained to solve the problem. The figure is recreated based on [100].

4) *Rubik's Cube Recovery*: This task combines the Jigsaw puzzle [78], slice order prediction [47], and rotation prediction [43] tasks. As shown in Fig. 7, it involves two operations: cube rearrangement and application of rotation, enabling the model to learn translational and rotational invariant features from volumetric data, such as 3D medical images [100]–[102]. A given sample \mathcal{V} with dimensions $W \times H \times L$ is divided into subcubes of size $W/n \times H/n \times L/n$, where n is the side length of each subcube. The initial configuration of these subcubes, determined by their order l and orientations g^{hor} and g^{ver} in the horizontal and vertical directions, respectively, represents the solved state (ground truth) of the Rubik's cube. A series of random volume-wise transformations, $\mathcal{T}(\mathcal{V})$, creates a Rubik's cube puzzle, $\tilde{\mathcal{V}}$, with the solved state serving as the ground truth for self-supervised training. The model is optimized by minimizing the objective function:

$$\mathcal{L}_{rubik} = \gamma \mathcal{L}_p + \eta \mathcal{L}_r, \quad (6)$$

where \mathcal{L}_p and \mathcal{L}_r are the order permutation and orientation loss, respectively, and γ and η control the relative weight of each term. When K rotations applied, and the model predicts ρ with one-hot label l , the order permutation loss is:

$$\mathcal{L}_p = - \sum_{i=1}^K l_i \log(\rho_i), \quad (7)$$

where l_i is the true label and ρ_i is the predicted probability for i th transformation. The orientation prediction is treated as a multi-class classification, where the model predicts the rotation status of each subcube. Let N be the number of subcubes, and g be the ground truth vector with 1 for rotated cubes and 0 otherwise. The model outputs two N -dimensional vectors, R^{hor} and R^{ver} , representing horizontal and vertical rotation probabilities, respectively. The orientation loss is defined as:

$$\mathcal{L}_r = - \sum_{n=1}^N [g_n^{hor} \log(R_n^{hor}) + g_n^{ver} \log(R_n^{ver})], \quad (8)$$

where g_n^{hor} and g_n^{ver} are the ground truth values for horizontal and vertical rotations, and R_n^{hor} and R_n^{ver} are the predicted probabilities.

Zhuang *et al.* [100] focus on hemorrhage classification and brain tumor segmentation in 3D medical images, where they use Rubik's cube recovery task to self-supervise a CNN. For classification, the CNN is fine-tuned directly on the target dataset. For segmentation, the pre-trained weights are adapted to the encoder, with feature maps expanded using dense upsampling Conv to generate pixel-wise predictions, replacing the ConvT used in standard encoder-decoder models. This reduces the trainable parameters and mitigates random initialization effects. Their results show improvements of 2.3% in brain tumor segmentation.

As an extension, [101] and [102] enhance this task by adding random cube masking. This modification leads to the updated objective function:

$$\mathcal{L}_{rubik} = \gamma \mathcal{L}_p + \eta \mathcal{L}_r + \delta \mathcal{L}_m, \quad (9)$$

where \mathcal{L}_p , \mathcal{L}_r , and \mathcal{L}_m represent the order permutation, orientation, and mask identification losses, respectively. The mask identification loss is a multi-classification problem:

$$\mathcal{L}_m = - \sum_{n=1}^N g_n^m \times \log(\rho_n^m), \quad (10)$$

with g_n^m indicating masked cube position and ρ_n^m being the predicted probability, for the n th subcube. This addition challenges the model to learn translation, rotation, and noise-invariant features. Unlike previous works, [102] employs a GAN-based architecture to combine Rubik's cube reconstruction and adversarial losses, improving SSL for 3D medical image segmentation. This approach increases the results of brain tissue segmentation in the MRBrainS18 [103] dataset by 3.97% in the dice score compared to training from scratch.

Limitations: While fine-tuning Rubik's cube recovery-based pre-trained models outperforms training-from-scratch models in tasks, like brain hemorrhage classification and tumor segmentation, this approach primarily captures spatio-global representations. Consequently, it may lack the fine-grained pixel-level details required for precise segmentation boundaries. Moreover, incorporating complexities, such as

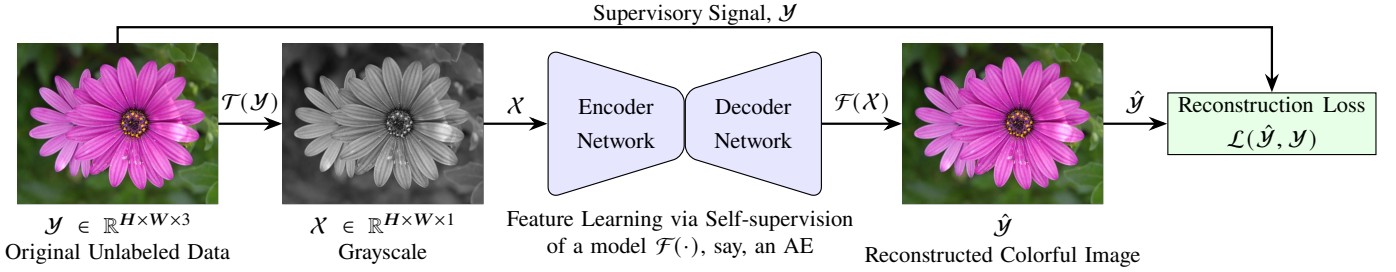


Fig. 8: Encoder-decoder network predicts the probable color from a grayscale image. $\mathcal{T}(\cdot)$ is an RGB to grayscale transformation.

subcube masking or adversarial learning can further increase the computational overhead of the self-supervision pipeline.

B. Generative Methods

In this pretext task, the model reconstructs the input, predicts missing parts (e.g., masked images or cloze tests in NLP [104]), or generates new data. These tasks range from low-level detail reconstruction to high-level semantic modeling. The methods train an encoder to map inputs to latent feature representations and a decoder to reconstruct them [105]–[107]. Advanced techniques, including adversarial learning, perceptual losses, and context encoders, are effective in capturing semantic information. However, simpler methods, like early GANs or AEs often struggle with long-range semantic relationships due to limited receptive fields or lack of contextual awareness. Recent innovations, viz. larger receptive fields, dilated convolutions, diffusion models [108], and attention mechanisms [109], improve the model’s ability to capture global context and semantic coherence [110], [111].

1) *Image Colorization*: It is a fundamental generative pretext task in SSL-based image segmentation [112], [113]. As shown in Fig. 8, it trains a model to generate a colorized image from a grayscale input, leveraging contextual cues, such as edges and object boundaries [114]. Given a grayscale input image, $\mathcal{X} \in \mathbb{R}^{H \times W \times 1}$, the objective is to learn a mapping $\hat{\mathcal{Y}} = \mathcal{F}(\mathcal{X})$ to the respective color image $\mathcal{Y} \in \mathbb{R}^{H \times W \times 3}$, where H, W are spatial dimensions of the input. If we consider the representation of the RGB image as a 3-dimensional space, then a natural objective function is the Euclidean loss $\mathcal{L}_2(\cdot, \cdot)$ between predicted and ground truth colors defined in (11).

$$\mathcal{L}_2(\hat{\mathcal{Y}}, \mathcal{Y}) = \frac{1}{2} \sum_{h,w} \|\mathcal{Y}_{h,w} - \hat{\mathcal{Y}}_{h,w}\|_2^2. \quad (11)$$

Although widely used in regression tasks, Euclidean loss in RGB space fails to capture multimodal color distributions due to the non-uniformity of RGB color perception. Perceptually uniform color spaces, such as CIE Lab [114], better align with human vision. Thus, multimodal color distributions are often modeled as a multinomial classification task over a quantized color set [114], [115]. For a given input \mathbf{X} , the model learns a mapping $\mathcal{Z} = \mathcal{G}(\mathbf{X})$, where $\mathcal{Z} \in [0, 1]^{H \times W \times Q}$ is the probability distribution over the Q quantized color at each pixel location (h, w) , satisfying $\sum_q \mathcal{Z}_{h,w,q} = 1$. The training objective is typically a multinomial cross-entropy loss:

$$\mathcal{L}_{cl}(\hat{\mathcal{Z}}, \mathcal{Z}) = - \sum_{h,w} v(\mathcal{Z}_{h,w}) \sum_q \mathcal{Z}_{h,w,q} \log(\hat{\mathcal{Z}}_{h,w,q}), \quad (12)$$

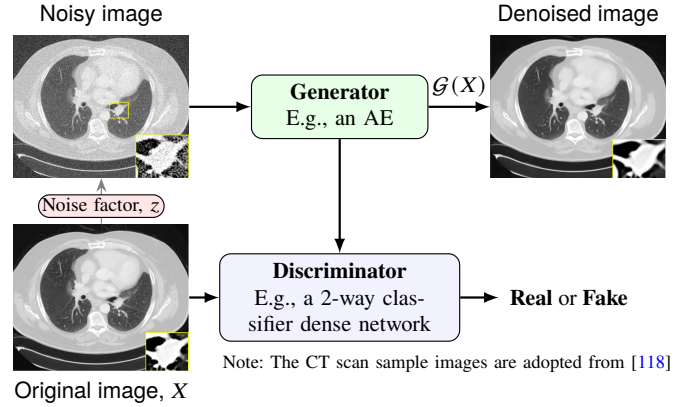


Fig. 9: Conceptual diagram of a GAN-based denoising.

where $\hat{\mathcal{Z}}$ and \mathcal{Z} denote the predicted and ground-truth color distributions, respectively. The term $v(\cdot)$ is a reweighting factor that adjusts the loss based on the rarity of specific color classes to mitigate the imbalance of classes. This framework can also be adapted for color correction tasks. For example, [116] presents a self-supervised GAN framework with CIE Lab color channel correction to learn light-invariant features for plant leaf segmentation. While colorization and color correction do not directly involve segmentation, they enable the model to distinguish regions and objects, aiding in contextual understanding. As a result, the learned features are effectively transferred to semantic segmentation tasks [113], [116], [117].

2) *Image De-noising*: It is typically tackled using models, like GANs similar to those used for image colorization [49], [50]. GANs, pioneered by [119], were extended by Luc *et al.* [120] to semantic segmentation and further developed by Hung *et al.* [121], Belagali *et al.* [122], and Li *et al.* [123], for semi-supervised segmentation. Fig. 9 illustrates a GAN-based framework, consisting of two modules: a generator \mathcal{G} , which maps noisy inputs X to denoised outputs $\mathcal{G}(X)$, and a discriminator D , which evaluates whether a sample belongs to the real data distribution.

The framework is trained using the adversarial loss function \mathcal{L}_{GAN} :

$$\mathcal{L}_{GAN}(G, D) = \mathbb{E}_x[\log D(x)] + \mathbb{E}_x[\log(1 - D(\mathcal{G}(x)))], \quad (13)$$

where $D(x)$ is the discriminator’s output for real samples, and $D(\mathcal{G}(x))$ is its output for the generator’s denoised prediction $\mathcal{G}(x)$. The generator learns to map noisy inputs to clean images, minimizing the discrepancy from the real data distribution $\mathbb{E}_x[\log(1 - D(\mathcal{G}(x)))]$, while the discriminator aims to

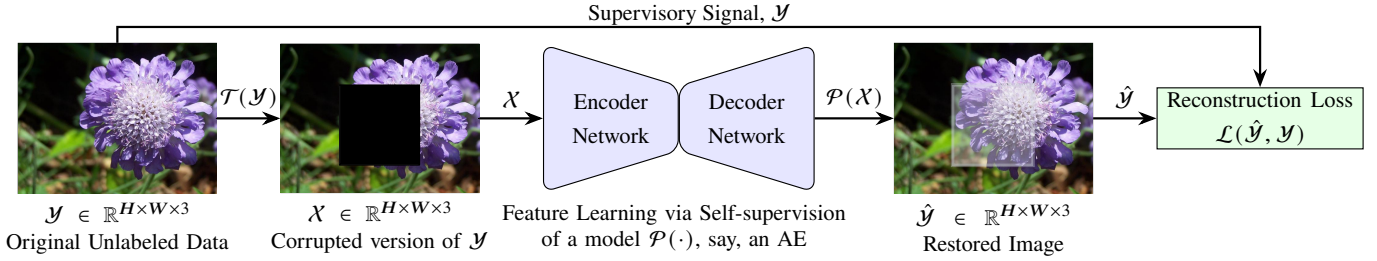


Fig. 10: The concept of the self-supervised image inpainting pre-training process using an AE.

distinguish between real and generated images by maximizing the term $\mathbb{E}_x[\log D(x)]$, the log probability of correctly classifying real samples. This adversarial optimization ensures the generator progressively improves its denoising capability. The generator can then be fine-tuned on domain-specific datasets. For example, [50] fine-tune it with limited labeled data for semantic segmentation, achieving competitive results. Beyond GANs, AEs are widely used for image denoising. Denoising autoencoders (DAEs) learn to reconstruct clean images from corrupted inputs. Their training objective, $\mathcal{L}(\theta)$, is typically defined as the mean squared error (MSE) between the input and its reconstructed output:

$$\mathcal{L}(\theta) = \frac{1}{N} \sum_{i=1}^N (f_{\theta}(x_i + \epsilon_i) - x_i)^2, \quad (14)$$

where $f_{\theta}(\cdot)$ is the DAE function, x_i is the input image, ϵ_i is added noise, and N is the number of training samples.

This approach has been successfully applied in microscopy data segmentation. For instance, [124], [125] use DAEs for nuclei segmentation, demonstrating that denoising pretext tasks improves segmentation accuracy. DAEs can also be trained with masked inputs, focusing loss computation on unmasked pixels, which enhances object boundary reconstruction. In medical imaging, Zhang *et al.* [67] propose a 3D-AE for self-supervised tumor segmentation in MRI. They reconstruct normal organs, tumors, and segmentation masks separately, using L1 loss for organ/tumor reconstruction and Dice loss for segmentation mask prediction. The overall objective is:

$$\mathcal{J} = \lambda_1 \mathcal{L}_{org} + \lambda_2 \mathcal{L}_{tum} + \lambda_3 \mathcal{L}_{dic}, \quad (15)$$

where \mathcal{L}_{org} and \mathcal{L}_{tum} are L1 reconstruction losses for normal and tumor regions, and \mathcal{L}_{dic} is the Dice loss for segmentation masks, with λ 's controlling the contribution of each term. They also incorporate transformations, elastic deformations, and Gaussian blurring to regulate the difficulty of self-supervision. Overall, both GANs and AEs are effective in SSL-based segmentation, as they learn robust representations while mitigating noise sensitivity. They also provide an efficient way to pre-train deep models on large-scale unlabeled data.

3) *Image Inpainting*: In this task, a model reconstructs missing regions of a corrupted image by predicting masked patches [45], [126]–[129], as illustrated in Fig. 10. This pretext task enables the model to learn intrinsic representations, capturing structured, semantically meaningful characteristics that improve contextual understanding and output quality. Re-

Algorithm 1 Image context swapping algorithm

```

1 def image_context_disordering(x_i, T):
2     # Input: x_i - Input image (array-like or tensor)
3     #         T - Number of iterations (int)
4     # Output: x_tilde_i - Img w/t disordered context
5
6     x_tilde_i = x_i.copy()
7
8     for iter in range(1, T + 1):
9         # Randomly select two non-overlapping
10         # patches from x_tilde_i
11         p1 = randomly_select_patch(x_tilde_i)
12         p2 = randomly_select_patch(x_tilde_i)
13
14         # Ensure the patches do not overlap
15         if not overlap(p1, p2):
16             # Swap the selected patches
17             swap(p1, p2)
18     return x_tilde_i
    
```

ferring to Fig. 10, the original image \mathcal{Y} undergoes corruption through a transformation function $\mathcal{T}(\cdot)$, defined as:

$$\mathcal{X} = \mathcal{T}(\mathcal{Y}) = M \odot \mathcal{Y}, \quad (16)$$

where \odot denotes element-wise multiplication, and $M \in \{0, 1\}^{H \times W}$ is a binary mask. Pixels with $M = 0$ are removed, while those with $M = 1$ are retained. In traditional inpainting, a model \mathcal{P} restores the original image by minimizing the normalized masked L_2 reconstruction loss:

$$\mathcal{L}_{rec}(\mathcal{X}) = \frac{1}{\sum(1 - M)} \|(1 - M) \odot (\mathcal{Y} - \mathcal{P}(\mathcal{X}))\|_2^2, \quad (17)$$

where $\sum(1 - M)$ normalizes the loss by the number of corrupted pixels. Research [45] suggests that L_1 and L_2 losses yield comparable performance, with selection depending on data characteristics. The study [127] showed that this pretext task enhances semantic segmentation of remote sensing images, particularly when fine-tuning with limited labeled data. Similarly, [128] demonstrated that self-supervised learning with Monte Carlo optimization improves human detection and segmentation. GAN-based approaches [130] have also been explored for inpainting. Performance can be further improved by modifying the masking function, integrating context-aware encoding, and employing attention mechanisms [131].

4) *Context Restoration*: It is built upon image inpainting and slice-order prediction techniques, involving two key sub-tasks: (i) identifying corrupted regions and (ii) reconstructing the correct image context. Instead of masking random regions, this method swaps the contexts of two non-overlapping regions, p_1 and p_2 ($p_1 \cap p_2 = \emptyset$), for T iterations, as detailed in

Algorithm 1. After the patch-swapping, the corrupted image is denoted as \tilde{X} . The model then learns the parameters θ by minimizing an appropriate loss function, like MSE (cf. (14)), to restore the original image ($\hat{X} = \mathcal{F}_\theta(\tilde{X})$). For instance, Chen *et al.* [132] applied this pretext task with 64×64 patches to enhance classification, segmentation, and localization in medical imaging modalities, viz. brain MRI, abdominal CT, and ultrasound spine coronal images. However, this approach has the following **limitations**: (i) selecting an appropriate patch size is crucial, as small patches may fail to capture strong contextual features, reducing the pretext task’s effectiveness; (ii) determining the optimal number of iterations is challenging, as excessive corruption can hinder the model’s ability to restore context, rendering the task counterproductive. Hence, pixel-wise generative SSL is computationally expensive and struggles to learn abstract latent patterns [26].

C. Contrastive Methods

Fig. 11 illustrates a general framework for contrastive learning, where a model is trained by minimizing the distance between positive (+ve) sample pairs, $\{x^+, x\}$, and maximizing the distance between negative (–ve) sample pairs, $\{x^-, x\}$, using the noise contrastive estimation (NCE) loss [44], [104], [133]:

$$\text{NCE}_{x, x^+, x^-} = -\log \left(\frac{e^{f(x)^\top f(x^+)}}{e^{f(x)^\top f(x^+)} + e^{f(x)^\top f(x^-)}} \right), \quad (18)$$

where $f(\cdot)$ is a vision encoder (e.g., ViT), x^+ is a similar sample to x , and x^- is a dissimilar sample. The NCE loss maximizes the softmax probability of the positive pair while minimizing it for the negative pair.

The selection of positive and negative samples plays a critical role. Positive pairs, $\{x_i, x_j\} \in \mathbb{X}$ are usually generated using random data augmentations from the same input. Because these two pairs originate from the same source, their features are expected to be close to each other in the feature spaces, h and z . Negative samples are the augmented views derived from different input samples in the same batch \mathbb{X} . Both augmented views x_i and x_j pass through a shared encoder (e.g., a DL backbone) to ensure consistency and alignment. The encoder maps the inputs to high-dimensional feature representations h_i and h_j , which are then projected into a lower-dimensional latent space via a projection head, typically a shallow neural network (e.g., an MLP), yielding z_i and z_j . The prediction head is optional. Some frameworks, such as bootstrap your own latent (BYOL) [134], introduce a prediction head to infer one view’s representation from the other. This approach is a defining characteristic of non-contrastive learning methods, where negative samples are not required. However, prediction heads can also be incorporated into contrastive frameworks. Finally, a contrastive loss is applied in the latent space, pulling +ve pairs $\{z_i, z_j\}$ closer, while pushing –ve pairs $\{z_i, z_k\}$ or $\{z_j, z_k\}$ apart, where z_k represents a –ve sample, to learn discriminative and invariant representations of the input. The standard NCE loss can be generalized to information noise-contrastive estimation (InfoNCE), which maximizes a lower

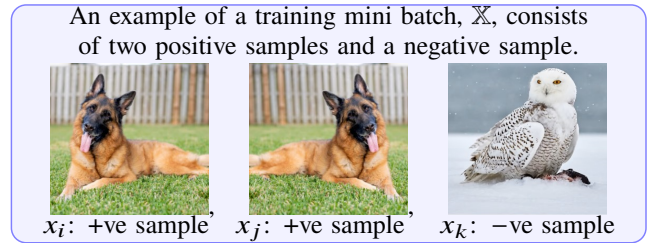
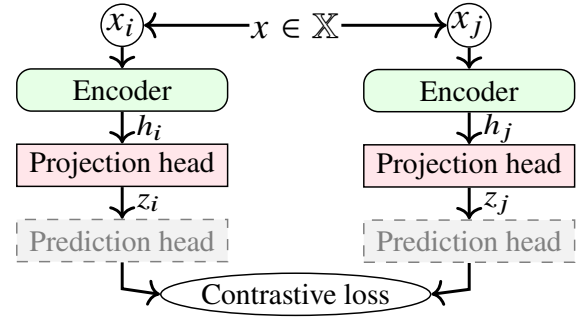


Fig. 11: The concept of self-supervised contrastive learning.

bound on mutual information by using multiple –ve samples (x_k^-) to improve discriminative power:

$$\text{InfoNCE}_{x, x^+, x_k^-} = -\log \left(\frac{e^{f(x)^\top f(x^+)}}{e^{f(x)^\top f(x^+)} + \sum_{k=1}^K e^{f(x)^\top f(x_k^-)}} \right). \quad (19)$$

While specific objective functions and feature extraction models may vary, the fundamental framework remains consistent. Several contrastive learning methods, including Deep InfoMax (DIM) [135], SimCLR [136], and MoCo [137], have been developed to enhance feature representation learning, achieving SOTA results across diverse domains. For instance, DIM maximizes mutual information between global and local features, while SimCLR and MoCo employ InfoNCE-based objectives to contrast positive and negative samples. Thus, contrastive learning has proven effective in leveraging synthetic or limited labeled data [138], [139], demonstrating its potential for generalizable image-level representation learning.

1) *Contrastive Predictive Coding (CPC)*: It was inspired by the InfoNCE loss and originally developed for learning representations from sequential data, like speech and text [104], [140]. It has since been extended to images to capture spatial information [141]. In CPC, an image is divided into overlapping patches $x_{i,j}$, where (i, j) denotes the spatial location. Each patch is encoded using a shared model, f_θ (e.g., ResNet), to produce feature maps $z_{i,j} = f_\theta(x_{i,j})$. These feature maps are processed by another model, g_ϕ (e.g., a masked CNN), to compute context vectors $c_{i,j}$, which depend only on past spatial locations ($u \leq i, v \leq j$), ensuring causality: $c_{i,j} = g_\phi(z_{u,v} | u \leq i, v \leq j)$. The goal is to predict ‘future’ feature maps $z_{i+k,j}$ from $c_{i,j}$ using a linear transformation with an embedding matrix W_k : $\hat{z}_{i+k,j} = W_k \cdot c_{i,j}$. A contrastive loss (20) enforces correct recognition of the target $z_{i+k,j}$ among randomly sampled negative feature maps z_l [141]:

$$\mathcal{L}_{\text{CPC}} = -\sum_{i,j,k} \log p(z_{i+k,j} | \hat{z}_{i+k,j}, \{z_l\}), \quad (20)$$

where

$$p(z_{i+k,j} | \hat{z}_{i+k,j}, \{z_l\}) = \frac{\exp(\hat{z}_{i+k,j}^\top z_{i+k,j})}{\exp(\hat{z}_{i+k,j}^\top z_{i+k,j}) + \sum_l \exp(\hat{z}_{i+k,j}^\top z_l)}$$

Extensions, such as [142], and [143] adapt CPC for semantic segmentation by learning dense, localized representations for spatial patches instead of global representations. These modifications enhance pixel-wise feature learning, improving segmentation performance on benchmarks, like Cityscapes [144], ADE20K [145], COCO Stuff [146], and PASCAL VOC [147]. For 3D data, conventional CPC shows poor results due to the fundamental differences between 2D images and 3D volumes, particularly in spatial dependencies and feature extraction [148]. To address this limitation, Zhu *et al.* [148] propose task-related CPC (TCPC), which integrates task-specific knowledge to enhance the representation learning. TCPC modifies the InfoNCE loss to differentiate positive samples (same context or structure) from negative ones. It employs supervoxel estimation to locate lesions and extracts features from sub-volumes around these regions, using a calibrated contrastive scheme for self-supervised learning. Experimental results show that integrating clinical priors, such as lesion positions, improves performance in 3D medical classification tasks (e.g., brain hemorrhage and lung cancer detection using CT scans), outperforming proxy tasks like 3D Jigsaw puzzles and Rubik’s cube solving.

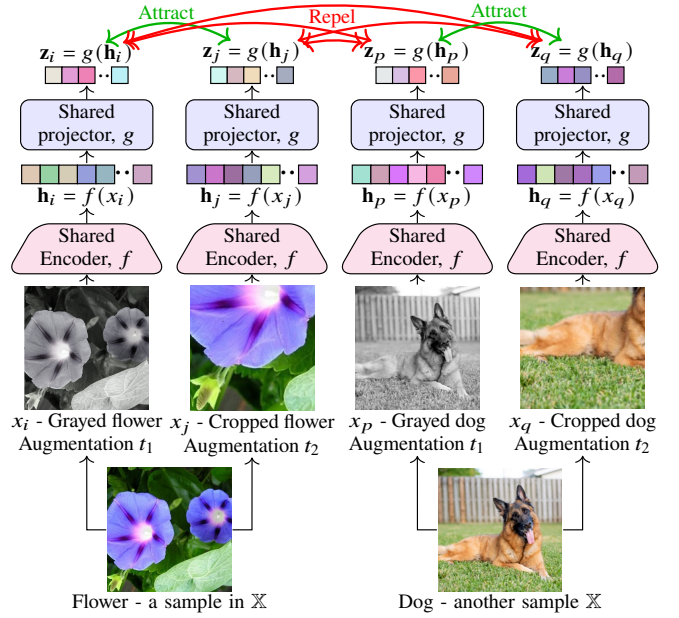
However, CPC and its variants have a few **limitations**: (i) It has difficulty capturing long-range dependencies, making it less effective for tasks requiring holistic scene understanding (e.g., object detection in cluttered images); (ii) By focusing on local patch, it may overfit to low-level features (e.g., textures) rather than learning high-level semantic representations transferable across tasks; (iii) Processing overlapping patches incurs high computational costs, exacerbated by contrastive loss calculations over multiple pair of samples.

2) *Simple Framework for Contrastive Learning (SimCLR)*: SimCLR simplifies the CPC pipeline by removing sequence prediction and focusing on instance discrimination. It learns invariant representations by maximizing agreement between two augmented views of the same image [136] as illustrated in Fig. 12.

During training, a minibatch \mathbb{X} of N images is sampled, and two random augmentations, $\mathcal{T} = \{t_1, t_2\}$, are applied to each image ($\tilde{x}_i = t_1(x)$, $\tilde{x}_j = t_2(x)$), generating $2N$ augmented samples. Given a positive pair $\{\tilde{x}_i, \tilde{x}_j\}$, the remaining $2N - 2$ samples act as negatives. A shared encoder, $f(\cdot)$, extracts features: $\mathbf{h}_i = f(\tilde{x}_i)$ and $\mathbf{h}_j = f(\tilde{x}_j)$. These are processed by a projection head, $g(\cdot)$, to obtain embeddings: $\mathbf{z}_i = g(\mathbf{h}_i)$ and $\mathbf{z}_j = g(\mathbf{h}_j)$. Training is guided by the normalized temperature-scaled cross-entropy loss (NT-Xent):

$$\mathcal{L}_{\text{SimCLR}}^{(i,j)} = -\log \frac{\exp(\text{sim}(\mathbf{z}_i, \mathbf{z}_j)/\tau)}{\sum_{k=1}^{2N} \mathbf{1}_{[k \neq i]} \exp(\text{sim}(\mathbf{z}_i, \mathbf{z}_k)/\tau)}, \quad (21)$$

where $\mathbf{1}_{[k \neq i]}$ ensures that the denominator excludes the similarity of \mathbf{z}_i itself, i.e., 1 if $k \neq i$, 0 otherwise, $\text{sim}(\cdot)$ is cosine similarity, and τ is a temperature parameter. After training, the projection head can be discarded to meet the needs of downstream tasks. Although originally designed for



Note: This figure is recreated based on Chen (2020)’s illustration of SimCLR [136]

Fig. 12: A SimCLR pipeline. The encoder and projector networks are trained together by minimizing a contrastive loss.

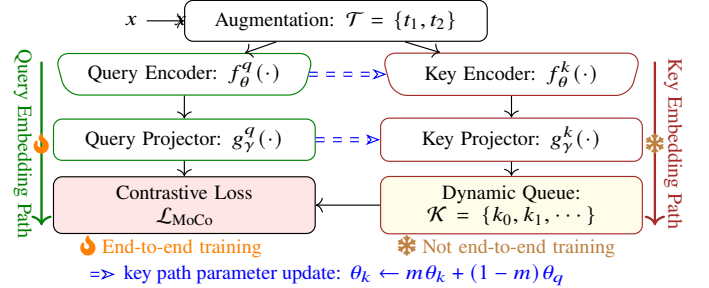


Fig. 13: An illustration of the MoCo pipeline.

classification, recent adaptations enable SimCLR for image segmentation [149]–[152], demonstrating its broader applicability. A key **limitation** of SimCLR is its dependence on large batch sizes to ensure sufficient negative samples, raising computational concerns. Hence, it is sensitive to the quality and diversity of applied augmentations.

3) *Momentum Contrast (MoCo)*: MoCo, like SimCLR, is an instance-based contrastive learning approach but estimates contrastive loss using one positive pair and K negative samples [137]. It maintains a dynamic queue as a memory bank, storing features (keys) from previous training iterations beyond the current mini-batch. The queue maintains a fixed size of K (e.g., 65,536) samples by removing the oldest keys on the fly. Unlike SimCLR, MoCo does not use shared networks for both views. Instead, it maintains separate networks for query and key embeddings, as illustrated in Fig. 13. Its training is asymmetric, i.e., only the query path, $f_\theta^q(\cdot) + g_\gamma^q(\cdot)$, is updated via backpropagation using a modified InfoNCE, while the key embedding path is updated via a momentum update with smoothing exponentially moving average (EMA). For instance, the key encoder parameter, θ^k , is updated as:

$$\theta_k \leftarrow m\theta_k + (1-m)\theta_q, \quad (22)$$

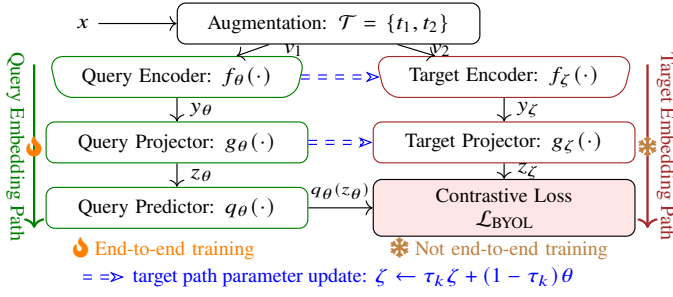


Fig. 14: An illustration of the BYOL pipeline. Note: This figure is inspired by Grill (2020) [134].

where $m \in [0, 1)$ is a momentum coefficient, and θ_q is the query encoder parameter. The same update rule applies to the key projection network, $g_k^k(\cdot)$. MoCo optimizes contrastive loss using the dynamic queue:

$$\mathcal{L}_{\text{MoCo}} = -\log \frac{\exp(\text{sim}(\mathbf{q}, \mathbf{k}^+)/\tau)}{\sum_{i=1}^K \exp(\text{sim}(\mathbf{q}, \mathbf{k}_i)/\tau)}, \quad (23)$$

where \mathbf{q} is the query representation, \mathbf{k}^+ is the positive key (an augmented view), \mathbf{k}_i are negative keys (from the queue), τ is a temperature parameter, and $\text{sim}(\cdot, \cdot)$ denotes cosine similarity.

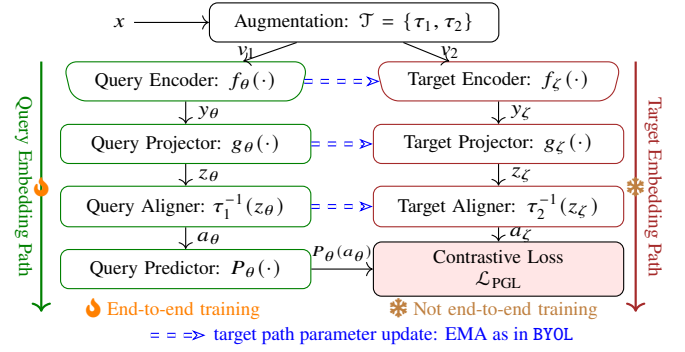
MoCo and its variants, including MoCo v2 [153], MoCo v3 [154], and Fast-MoCo [155], have demonstrated effectiveness in semantic segmentation. These methods outperform fully supervised training across data types, viz. natural images, medical imaging, and Lidar point clouds [137], [153]–[158].

MoCo’s **limitations** are: (i) The dynamic queue increases memory usage and computational overhead, making it resource-intensive; (ii) Maintaining separate query and key networks adds computational and implementation complexity compared to SimCLR’s shared network; (iii) Sensitivity to the momentum coefficient m poses challenges—high m slows adaptation, while low m risks instability.

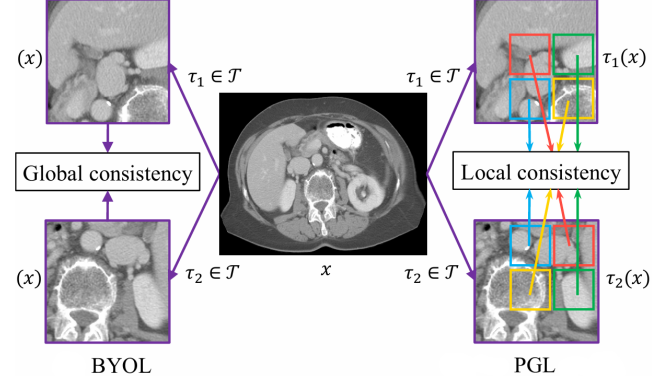
4) *Bootstrap Your Own Latent (BYOL)*: While traditional contrastive learning methods (e.g., SimCLR, or MoCo) rely on distinguishing +ve and –ve pairs, BYOL adopts a self-distillation approach that learns without –ve samples by using only +ve pairs [134]. This is achieved through an additional prediction head, $q_\theta(\cdot)$, on top of the query projection head, as shown in Fig. 14. The prediction head aligns query and target embeddings while preventing representation collapse. The target network mirrors the query path, consisting of an encoder $f_\zeta(\cdot)$ and a projector $g_\zeta(\cdot)$, but with separate parameters ζ . The query network (encoder, projector, and predictor) is updated via backpropagation, while the target network is updated solely through EMA of the query parameters. At training step k , for a momentum decay rate $\tau_k \in [0, 1)$, the update rule is:

$$\zeta \leftarrow \tau_k \zeta + (1 - \tau_k) \theta. \quad (24)$$

During training, an image x is transformed into two augmented views, v_1 and v_2 , using augmentation $\{t_1, t_2\} \sim \mathcal{T}$. The query path computes the encoder features $y_\theta = f_\theta(v_1)$, projection map $z_\theta = g_\theta(y_\theta)$, and prediction $q_\theta(z_\theta)$. The target path processes v_2 to produce $y_\zeta = f_\zeta(v_2)$ and projection



(a) An illustration of the PGL pipeline inspired by Xie (2020) [26].



(b) Concept of BYOL and PGL. This fig. is adopted from [26].

Fig. 15: The concept of the PGL.

$z_\zeta = g_\zeta(y_\zeta)$. The loss function is the mean squared error between the ℓ_2 -normalized prediction and target projection:

$$\mathcal{L}_{\text{BYOL}} = 2 - 2 \cdot \frac{\langle q_\theta(z_\theta), z_\zeta \rangle}{\|q_\theta(z_\theta)\|_2 \cdot \|z_\zeta\|_2}, \quad (25)$$

where $\langle \cdot, \cdot \rangle$ denotes cosine similarity. Minimizing $\mathcal{L}_{\text{BYOL}}$ enhances alignment between query and target projections, with zero loss indicating perfect alignment.

Initially proposed for image classification, BYOL has been extended to image segmentation [134], [159], [160], object detection [161], and monocular depth estimation [134]. However, BYOL has the following **limitations**: (i) Like MoCo, its dual-network design increases computational and memory overhead; (ii) Relying solely on positive samples may limit its ability to learn discriminative features, particularly in diverse or complex datasets; (iii) Its global instance-level representations may be suboptimal for tasks like semantic segmentation that require local cues, necessitating adaptations of multi-scale learning or spatial constraints; (iv) Sensitive to the momentum coefficient used in target network updates.

5) *Prior-Guided Local (PGL)*: SimCLR and BYOL primarily focus on global feature consistency, often overlooking local feature alignment. However, learning local regional representations enhances the structural understanding, making models more effective for segmentation tasks, as illustrated in Fig. 15. To address this, Xie *et al.* [26] introduced an additional *aligner* layer after the projection head in both query and target paths, modifying the BYOL pipeline (cf. Fig. 15a). The aligner exploits augmentation information (e.g., flipping, cropping,

scaling) to align features extracted from different views of the same region (cf. Fig. 15b). The augmentation module generates two views of an image: $v_1 = \tau_1(x)$ and $v_2 = \tau_2(x)$. The query and target paths produce feature representations: $z_\theta = g_\theta(f_\theta(v_1))$, and $z_\zeta = g_\zeta(f_\zeta(v_2))$, where θ and ζ are the parameters of the query and target networks, respectively.

The alignment modules reverse the applied transformations: $a_\theta = \tau_1^{-1}(z_\theta)$, and $a_\zeta = \tau_2^{-1}(z_\zeta)$, utilizing prior knowledge of τ_1 and τ_2 . Ideally, these features represent the same local region of the input image. The predictor head $P_\theta(\cdot)$ in the query path then predicts the target aligner’s output. The model is optimized by minimizing the local consistency loss:

$$\mathcal{L}_{\text{local}}(v_1, v_2) = \frac{\sum \|\mathcal{N}(P_\theta(a_\theta)) - \mathcal{N}(a_\zeta)\|_2^2}{K \times H \times W \times D}, \quad (26)$$

where \mathcal{N} represents ℓ_2 normalization along the channel axis, and K, H, W, D denote the batch size, height, width, and depth of the aligner features, respectively. Similarly, when v_2 is fed into the query network and v_1 into the target network, the loss is defined as $\mathcal{L}_{\text{local}}(v_2, v_1)$. The total loss minimized is:

$$\mathcal{L}_{\text{PGL}} = \mathcal{L}_{\text{local}}(v_1, v_2) + \mathcal{L}_{\text{local}}(v_2, v_1). \quad (27)$$

Similar to BYOL, only the query path undergoes end-to-end training, while the target path is updated via EMA. PGL and its variants have demonstrated competitive performance in segmentation tasks across natural images, remote sensing, and 3D medical imaging [26], [77], [162]–[166].

Despite its advantages, PGL has the following **limitations**: (i) The addition of aligner modules increases computational overhead, particularly for high-resolution images. (ii) It relies on augmentation priors and transformation reversals to align local features, which may not always be accurately defined in real-world applications. (iii) In datasets with fine-grained details, such as medical or remote sensing images, misalignment between augmented views can degrade feature consistency. (iv) Its performance is sensitive to hyperparameters, including patch sizes, augmentation strategies, and the trade-off between local and global consistency in the loss function.

6) *Swapping Assignments between multiple Views (SwAV)*: Unlike MoCo, BYOL, or PGL, SwAV does not maintain separate query and target networks. Instead, it uses a shared network, akin to SimCLR, as shown in Fig. 16. Unlike SimCLR, SwAV introduces a prototype layer in place of the projection layer and minimizes a unique loss function designed to dynamically balance cluster assignments [167]. It learns the input representations by comparing cluster assignments across different views rather than directly contrasting their features. Given an input x , random transformations t_1 and t_2 (e.g., cropping, aspect ratio changes) produce two augmented views, v_1 and v_2 . Both views pass through a shared encoder $f_\theta(\cdot)$, yielding feature embeddings z_1 and z_2 . These embeddings are then projected onto K trainable prototype vectors, C_k , forming dot products $z_1^T C_k$ and $z_2^T C_k$. The resulting projections (prototype representations) are mapped to soft cluster assignments \mathbf{q}_1 and \mathbf{q}_2 via the Sinkhorn-Knopp algorithm [168].

SwAV’s core mechanism is swapped prediction: $\mathbf{z}_1^T C_k$ predicts \mathbf{q}_2 , and $\mathbf{z}_2^T C_k$ predicts \mathbf{q}_1 . Since both views originate from the same image, their features should encode similar

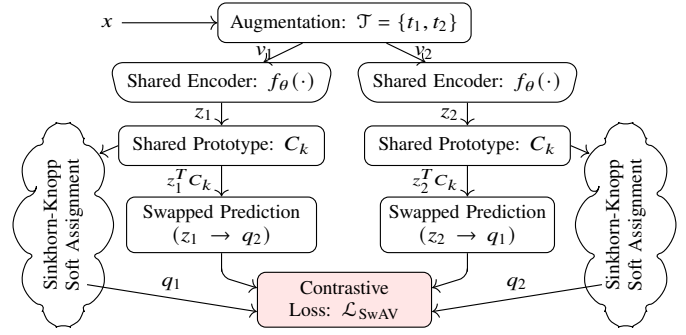


Fig. 16: An illustration of the SwAV pipeline.

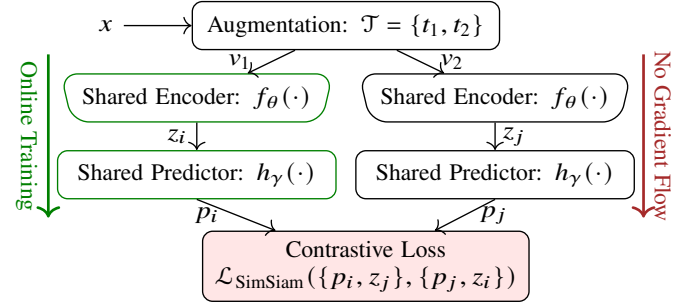


Fig. 17: SimSiam’s overview based on pseudocode of [73].

features, allowing cross-view prediction of cluster assignments. The training minimizes the discrepancy between predicted and actual assignments using a cross-entropy (CE) loss:

$$l_{\text{CE}}(\mathbf{z}_1, \mathbf{q}_2) = - \sum_{k=1}^K \mathbf{q}_2^{(k)} \log \frac{\exp(\frac{1}{\tau} \mathbf{z}_1^T C_k)}{\sum_{k'=1}^K \exp(\frac{1}{\tau} \mathbf{z}_1^T C_{k'})}, \quad (28)$$

where τ is a temperature parameter controlling the sharpness of the softmax distribution. A similar loss $l_{\text{CE}}(\mathbf{z}_2, \mathbf{q}_1)$ is defined for the second view. Thus, the total loss function is:

$$\mathcal{L}_{\text{SwAV}} = l_{\text{CE}}(\mathbf{z}_1, \mathbf{q}_2) + l_{\text{CE}}(\mathbf{z}_2, \mathbf{q}_1). \quad (29)$$

Minimizing $\mathcal{L}_{\text{SwAV}}$ jointly updates the encoder parameters, θ , and the prototype matrix, C , allowing prototypes to adapt dynamically during training [167].

However, one must be aware of SwAV’s **limitations** before applying it to a problem domain: (i) While effective on large-scale datasets (e.g., ImageNet), performance degrades on smaller datasets; (ii) Success depends on generating diverse and meaningful augmented views for robust cluster assignments; (iii) Clustering-based pseudo-labels struggle to capture fine-grained class distinctions in highly diverse datasets; (iv) Its global-level representation learning may not provide optimal features for dense prediction tasks without domain-specific adaptation; (v) The multi-crop augmentation strategy increases computational overhead during training.

7) *Simple Siamese Representation Learning (SimSiam)*: Fig. 17 illustrates the workflow of SimSiam, a simplified variant of SimCLR [136], BYOL [134], and SwAV [167]. It has several distinguishing features: (i) Unlike MoCo, BYOL, and PGL, SimSiam removes the momentum encoder, relying solely on shared weights for both branches. (ii) Like SimCLR and SwAV, it shares the encoder and predictor across both

branches but introduces asymmetry via a stop-gradient applied to one branch. (iii) Unlike SimCLR, SimSiam does not use $-ve$ pairs, and unlike SwAV, it does not involve clustering or prototypes. Instead, it relies solely on $+ve$ pairs and the stop-gradient operation to prevent collapse.

Given an input x , two augmented views v_1 and v_2 are generated. A shared encoder $f_\theta(\cdot)$ processes these views, yielding feature representations z_i and z_j . A shared predictor then maps z_i to a prediction $p_i = h(z_i)$. Training minimizes the negative cosine similarity between p_i and z_j :

$$S_{cos}(p_i, z_j) = -\frac{p_i}{\|p_i\|_2} \cdot \frac{z_j}{\|z_j\|_2}, \quad (30)$$

where $\|\cdot\|_2$ denotes the ℓ_2 -norm. The total symmetric loss is:

$$\mathcal{L} = \frac{1}{2}S_{cos}(p_i, z_j) + \frac{1}{2}S_{cos}(p_j, z_i), \quad (31)$$

averaged over all samples. The online branch is trained via backpropagation, while the other branch remains fixed (i.e., no gradient updates or momentum-based updates).

SimSiam has been used to pre-train models, enabling the extraction of transferable features for various downstream tasks. In the original study [73], SimSiam was evaluated on object detection and instance segmentation benchmarks, including Pascal VOC [169] and MS COCO [170]. Results demonstrated competitive performance against contemporary SSL methods, highlighting SimSiam’s effectiveness. Its advantages—particularly the elimination of $-ve$ pairs and its ability to train with small batch sizes—make it well-suited for semantic segmentation [149], [171]–[173]. For example, Wang *et al.* [172] applied SimSiam to histopathology image segmentation, reporting superior performance over other SSL approaches. Similarly, Gandhi *et al.* [149] used SimSiam with a ResUNet++ [174] backbone for land cover segmentation in satellite imagery. Their findings show that SimSiam outperforms SimCLR when using only 50% of labeled data. Additionally, Sakaguchi *et al.* [173] integrated SimSiam into an object instance retrieval framework for assistive robotics, exploiting 3D semantic map views to enhance performance.

Limitations of SimSiam are: (i) The absence of negative samples makes performance highly sensitive to architecture and data augmentation choices, with suboptimal configurations leading to degraded results. (ii) The stop-gradient mechanism, while preventing representation collapse, may require extensive fine-tuning for specific tasks, adding computational overhead. (iii) It has mainly been validated on modest backbone architectures; its scalability to large datasets and high-capacity models (e.g., transformers) remains underexplored.

D. The Emerging Ideas

Numerous studies have demonstrated the effectiveness of self-supervised learning (SSL) in image segmentation tasks, achieving performance comparable to fully supervised methods while significantly reducing the need for labeled data. However, most SSL approaches are designed to learn global representations, which may be suboptimal for dense prediction tasks, like semantic segmentation [14], [163]. To address

this limitation, recent advancements focus on dense SSL approaches, either at the pixel-level [142], [175], [176] or region-level [177], [178]. For instance, DenseCL [142] extends MoCo v2 [153] by introducing dense pairwise contrastive learning at the pixel-level. DenseSiam [179] employs a dense Siamese network that exploits both pixel and region consistency for enhanced dense feature learning. Chaitanya *et al.* [180] come up with a local contrastive loss that enforces similarity between transformed local regions while ensuring dissimilarity with other areas of the same image. The local contrastive loss for a given similar image pair, $\{\tilde{x}, \hat{x}\}$ of size $W_1 \times W_2 \times C$, is defined as:

$$l(\tilde{x}, \hat{x}, u, v) = -\log \frac{\exp[\text{sim}(\tilde{f}(u, v), \hat{f}(u, v))/\tau]}{\exp[\text{sim}(\tilde{f}(u, v), \hat{f}(u, v))/\tau] + \Gamma}, \quad (32)$$

where $\text{sim}(\cdot, \cdot)$ is the cosine similarity, τ is a temperature parameter—a smaller τ emphasizes the difference in similarity, which helps the loss focus more on the most similar pairs and the hardest dissimilar pairs. (u, v) indexes local regions in the feature maps, $f(u, v) \in \mathbb{R}^{K \times K \times C}$, forming the similar pair set Ω^+ , and Γ is defined as:

$$\Gamma = \sum_{(u', v') \in \Omega^-} \exp[\text{sim}(\tilde{f}(u, v), \hat{f}(u', v'))/\tau],$$

where Ω^- denotes the dissimilar set consisting of all other local regions in both feature maps, \tilde{f} and \hat{f} . Thus, the total local contrastive loss, when each feature map is divided into D local regions, each of size $K \times K \times C$, with $K < \min(W_1, W_2)$, for a set of images from \mathbb{X} , can be defined as:

$$L_l = \frac{1}{|\mathbb{X}|} \sum_{x \in \mathbb{X}} \frac{1}{D} \sum_{(u, v) \in \Omega^+} [l(\tilde{x}, \hat{x}, u, v)]. \quad (33)$$

Experimental studies demonstrate that incorporating local contrastive loss improves MRI image segmentation over traditional approaches [175], [180]. Likewise, Xie *et al.* [26] explore region-wise local consistency in the latent space of SSL for medical image semantic segmentation. Islam *et al.* [181] introduce a pixel-level contrastive loss into BYOL, enhancing dense feature representations for downstream tasks of object detection and semantic segmentation. Another work in [77] proposes a novel SSL framework for medical image segmentation, termed cross-modal alignment and deep self-distillation (CADS). This method integrates concepts from CPC and BYOL, formulating a hybrid SSL approach. The cross-modal alignment component utilizes a differentiable projection module to generate digitally reconstructed radiographs (DRRs) from 3D CT volumes, serving as X-ray proxies. This alignment enables effective feature learning across 2D and 3D modalities. Meanwhile, the deep self-distillation component employs a teacher-student framework, refining hierarchical feature representations similar to BYOL. By aligning features across modalities, CADS enhances modality-invariant feature learning, which is crucial for volumetric medical image segmentation that requires spatial and contextual understanding in 3D data. While CADS achieves promising results on CT scan segmentation, its performance remains sensitive to input image/patch size and lacks generalizability across different imaging modalities and tasks.

TABLE II: Comparison of popular predictive and generative self-supervised learning approaches.

	Pretext Task	Description	Key Characteristics
Predictive SSL	Slice Order	Divide an image into random slices for reordering	Simple to implement but sensitive to slice order, leading to artifacts
	Jigsaw Puzzle	Divides an image into patches, rearranges them randomly, and trains the model to predict the original positions, enhancing spatial relationship learning	Improves spatial understanding but requires high computation and large datasets
	Rubik’s Cube	Simulates a 3D Rubik’s Cube by rotating and permuting image patches, training the model to predict both transformations	Trains the model on spatial and orientation-aware features, but computational complexity increases significantly due to the 3D nature of the task
	Rotation Prediction	Rotates an image along horizontal axes and trains the model to predict the rotation, enhancing orientation-invariant learning	Simple and effective for orientation learning, but limited to discrete rotations
Generative SSL	Denoising	Learns to reconstruct clean images from noisy inputs, encouraging the model to extract robust features	Utilizes large unlabeled datasets; effective for noise removal but sensitive to noise types and levels
	Colorization	Predicts realistic colors for grayscale images by learning contextual and semantic features	enhances understanding of object semantics but may require post-processing for accurate results
	Inpainting	Predicts missing or occluded regions in an image by leveraging surrounding contextual information	Improves spatial and contextual feature learning; effective for object removal and photo restoration but may struggle with complex or large missing areas
	Context Restoration	Trains the model to restore or predict spatial relationships and contextual consistency within an image	Enhances the model’s ability to capture object relationships and spatial structure; may require complex training procedures
Contrastive SSL	CPC	Maximizes mutual information across views	State-of-the-art results; limited spatial focus
	SimCLR	Maximizes intra-image similarity across views	Versatile but computationally expensive
	MoCo	Uses memory bank for feature updates	Efficient memory use; high data requirements
	PGL	Learns graph-based patch relationships	Captures spatial relations; costly for large datasets
	BYOL	Uses consistency loss across augmentations	Memory-efficient; sensitive to hyperparameters
	SwAV	Multi-crop augmentations for representation learning	Good for transfer learning; computationally heavy
	SimSiam	Two-branch network with stop-gradient	Simple, scalable; less effective for low-diversity datasets

TABLE III: Comparison of popular contrastive learning approaches based on key features.

Feature	SimCLR	MoCo	BYOL	PGL	SwAV	SimSiam
Methodology	Contrastive learning with large batches	Momentum contrast mechanism	Negative-sample-free, self-distillation, momentum update	Prior-guided local alignment for segmentation tasks	Online clustering with Sinkhorn-Knopp algorithm	Negative-sample-free, no momentum update, stop-gradient
Architecture	Encoder + Projection	Encoder + Memory Queue	Student + Teacher	Aligner modules with query/target paths	Encoder + Prototype layer	Encoder + Projection head
Learning Objective	Contrastive loss	Contrastive loss	Self-distillation	Local and global consistency loss	Swapped prediction with clustering	Self-distillation
Negative Samples	Required (minibatch)	Required (memory bank)	Not required	Not required	Not required (clustering instead)	Not required
Dependence on Batch	High	Low (memory bank)	None	Medium	Low	Low
Simplicity	Moderate	Complex	Simple	Moderate	Moderate	Simple
Strengths	Simplicity, scalable	Memory-efficient, suitable for smaller batches	No negative samples, avoids batch size constraints	Captures local structural information, ideal for segmentation	Balanced clustering, robust to batch sizes	Easy to implement, small batch sizes, no negative samples
Limitations	Requires large batch sizes	Requires a memory queue	Sensitive to augmentation strategy	Computational overhead due to aligners; depends on priors	Sensitive to clustering hyperparameters	Sensitive to architecture and augmentation

E. Summary

Table II and Table III summarize the details of the three categories of SSL—predictive, generative, and contrastive learning—pretext tasks, offering a concise breakdown of their characteristics and applications. Furthermore, Table III provides a comparative overview of the contrastive SSL methods discussed in this study, evaluated in eight key properties.

IV. COMMONLY USED DATASETS

The advancement of image segmentation has been driven by benchmark datasets released by various groups and institutions

that facilitate model development, evaluation, and standardized analysis. This section summarizes commonly used datasets and their properties. Table IV provides an overview of some publicly available benchmark datasets for segmentation.

A. Medical Imaging Datasets

KiTS 2023 [182]: It is the 3rd iteration of the Kidney Tumor Segmentation (KiTS) Challenge organized by the University of Minnesota, the German Cancer Research Center (DKFZ), and the Cleveland Clinic’s Urologic Cancer Program. It provides

TABLE IV: Widely used publicly available datasets for semantic segmentation research and development.

Dataset	Description	Image Resolution	# of Samples	# of Classes
KiTS 2023 [182]	Kidney CT scans with a ternary mask identifying semantic segmentation of kidneys, renal tumors, and renal cysts. 489 cases are allocated to the training and 110 cases are for testing sets.	Variable	599	3
BraTS 2024 [183]	Brain MRIs with detailed voxel-level annotations for enhancing tumor, non-enhancing tumor core, and surrounding FLAIR hyper-intensity, consisting of 500, 70, and 180 samples for training, validation, and testing, respectively.	Variable	750	3
ISIC 2018 [184]	DICOM skin imaging for skin lesion segmentation and classification. Image-level labels and pixel-level segmentation masks are provided for lesion segmentation (3,694) and 5-way lesion attribute detection (3,694), and 7-way lesion disease classification (11,720).	1024 × 1024	18,108	2/5/7
Cityscapes [144]	Urban street scenes with detailed dense pixel-level annotations for various objects.	2048 × 1024	5,000	30
CamVid [60]	Urban scene understanding dataset with pixel-wise semantic segmentation.	960 × 720	701	32
SYNTIA [185]	Photo-realistic synthetic urban scenes of random snapshots and video sequences. Includes different seasons, weather, and illumination conditions from multiple viewpoints with pixel-level annotations.	1280 × 960	213,400+	13
ADE20K [145]	A comprehensive dataset with 150 object semantic segmentation masks, with 20,000 images for training, 2,000 images for validation, and 2,000 images for testing.	Variable	20,000+	150
PASCAL VOC [186]	Popular dataset for object recognition and segmentation with pixel-level annotations.	Variable	11,530	20
MS COCO [170]	Contains detailed pixel-level masks for 80 diverse objects in various backgrounds.	Variable	330,000	80

high-quality segmentation annotations of kidneys, kidney tumors, and kidney cysts composed of 599 cases (training set - 489 and test set - 110). The current SOTA model achieves a Dice score of 83.5% according to [KiTS leaderboard](#).

BraTS 2024 [183]: It is the 13th iteration of the long-standing Brain Tumor Segmentation (BraTS) Challenge, which has been held annually since 2012. Over the years, BraTS has expanded its scope to address various clinical concerns and tumor types as part of its ongoing efforts to advance automated brain tumor segmentation. It provides a labeled dataset consisting of 500, 70, and 180 samples for training, validation, and testing, respectively. However, researchers can utilize previous versions that contain additional training samples to enhance their model performance. The current SOTA model achieves a Dice score of 89.4% according to the [BraTS leaderboard](#).

ISIC 2018 [184]: The 2018 International Skin Imaging Collaboration (ISIC) Challenge is the 3rd iteration, held at MICCAI, aimed to advance AI-driven dermatological analysis. It has 3 tasks: (i) *Binary lesion segmentation*: Training set contains 2,594 dermoscopic images with segmentation masks. The validation and test sets include 100 and 1,000 images, respectively, without ground truth masks. (ii) *5-way lesion detection*: It involves detecting 5 dermoscopic attributes. The training set has 2,594 images w/t 12,970 segmentation masks (5 per image). The validation and test sets have 100 and 1,000 images, respectively, without ground truths. (iii) *7-way lesion classification*: Training set has 10,015 images w/t labels for 7 disease types. The validation and test sets have 193 and 1,512 images, respectively, without ground truths. The [ISIC 2018 leaderboard](#) shows the model that performed the best in the segmentation task and achieved a Jaccard index of 80.2%. In later iterations, the focus shifted toward classification tasks.

B. Urban Scene Understanding Datasets

CamVid [60]: The Cambridge-driving Labeled Video Database (CamVid) is a pioneering dataset for semantic segmentation in driving scenarios. It consists of 5 video sequences captured using a 960 × 720 resolution camera mounted on a vehicle’s dashboard. From these sequences, 701 frames were

manually annotated, with each pixel assigned to one of the 32 semantic classes. A common split includes 367 training, 101 validation, and 233 test images. According to [recent evaluations](#), the SOTA model SERNet-Former has achieved a mean intersection over union (mIoU) of 84.6%.

Cityscapes [144]: It is a large-scale dataset for semantic and instance segmentation in urban street scenes, widely used in autonomous driving research. It helps in understanding the driving environment, pedestrian detection, and traffic analysis, supporting self-driving cars and intelligent transportation systems. The dataset includes high-resolution images from 50 cities, covering diverse urban environments with 30 semantic classes. It provides 5,000 finely annotated images and 20,000 coarsely annotated images, enabling both detailed analysis and large-scale training. Coarse annotations can be used for pre-training, followed by fine-tuning on finely annotated images to improve model performance. The current state-of-the-art model on the Cityscapes benchmark achieves a mIoU of 86.7% according to [Cityscapes leaderboard](#). Its latest version provides 3D bounding box annotations for all vehicles in the original Cityscapes samples and a benchmark for 3D detection.

SYNTIA 2016 [185]: The SYNTHetic collection of Imagery and Annotations (SYNTIA) is a dataset designed to aid semantic segmentation and scene understanding in driving scenarios. It comprises over 200,000 high-definition images from video streams and more than 20,000 HD images from independent snapshots, all rendered from a virtual city with precise pixel-level semantic annotations for 13 classes. This dataset covers various conditions lighting, and weather (dynamic lights, shadows, multiple daytime modes, rain, etc.). The SOTA model, [SSMA](#), achieves an mIoU of 91.3% on the SYNTIA dataset. The latest version, SYNTIA-AL 2019, extends the number of classes to 15 and provides additional annotations, including instance segmentation, 2D and 3D bounding boxes, and depth information.

C. General Purpose and Specialized Datasets

ADE20K [145]: It is a comprehensive collection of over 27,000 images sourced from the SUN and Places databases,

meticulously annotated to include more than 3,000 object categories. The dataset is divided into 25,574 images, and 2,000 images for training and validation, respectively. As of the [latest evaluations](#), the SOTA model on the ADE20K dataset is ONE-PEACE with an mIoU of 63%.

PASCAL VOC [186]: The PASCAL Visual Object Classes (VOC) dataset, introduced in 2005, has been a cornerstone in advancing object recognition and semantic segmentation research. The 2012 iteration, PASCAL VOC 2012, comprises 11,530 images annotated with 20 object categories, including vehicles, animals, and household items. Over the years, PASCAL VOC 2012 has served as a benchmark for various semantic segmentation models. Notably, SegNext achieved an mIoU of 90.60% according to [PASCAL VOC leaderboard](#).

MS COCO [170]: The Microsoft Common Objects in Context (MS COCO) dataset is a comprehensive resource extensively utilized in computer vision research, particularly for semantic segmentation. It comprises over 330,000 images, with more than 200,000 labeled, encompassing 1.5M object instances across 80 object categories. Each image is annotated with pixel-level segmentation masks. In recent advancements, the [Co-DETR](#) model has achieved SOTA performance with an mIoU of 57.10% on the COCO test benchmark for instance segmentation. This model leverages a transformer-based architecture to enhance object detection and segmentation capabilities, demonstrating significant improvements in accuracy.

V. CHALLENGES AND FUTURE RESEARCH DIRECTIONS

A. Challenges

Self-supervised image segmentation is an emerging research area in computer vision that seeks to address the limitations of traditional supervised segmentation methods, which rely on large amounts of labeled data. Although SSL has made significant progress, identifying an optimal pretext task tailored to specific downstream segmentation applications remains challenging. The **challenges** can be summed as:

- (i) *Limited labeled data* - Since self-supervised methods do not rely on annotations, benchmarking and comparing different approaches is difficult due to the scarcity of labeled datasets.
- (ii) *Defining meaningful objectives* - Designing self-supervised objectives that effectively capture structural patterns while remaining generalizable across datasets is challenging.
- (iii) *Sensitivity to initialization and hyperparameters* - Training stability and performance are highly dependent on initialization and hyperparameter tuning, leading to potential instability.
- (iv) *Capturing complex relationships* - Many self-supervised approaches primarily employ local and low-level features, limiting their ability to model high-level contextual relationships.
- (v) *Interpretability and generalization* - Self-supervised models often lack interpretability and may struggle to generalize to unseen data, restricting their practical applicability.

B. Future Research Directions

In light of the above challenges, self-supervised image segmentation remains an active research area, offering promising opportunities for improvement and innovation. For instance, [98] proposed a network, integrating SSL with supervised

learning, with a shared backbone for both ways of learning: one branch performing 4-way rotation prediction as in SSL and another conducting n -way classification as in supervised learning, where the backbone is optimized using a combined loss from both tasks. More similar innovations and continued research are necessary to advance self-supervised segmentation. Here are some potential **future research directions**:

- (i) *Incorporating Semantic Information* - Most self-supervised segmentation methods focus on predicting spatial relationships within an image. Incorporating semantic information (e.g., object labels) into the SSL process could enhance accuracy and interpretability.
- (ii) *Domain Adaptation* - Self-supervised segmentation models are typically trained on large datasets and then applied to unseen data. However, performance may degrade when applied to datasets with domain shifts. Developing domain adaptation techniques could improve model generalization.
- (iii) *Few-Shot/ Zero-Shot Learning* - Extending the models to operate in few-shot and zero-shot settings would enable them to segment objects with minimal or no labeled examples, broadening their practical applicability.
- (iv) *Weakly-Supervision* - Combining SSL with weak supervision, where a small amount of labeled data guides the learning process, could enhance segmentation results.
- (v) *Interactive Methods* - Developing self-supervised models capable of incorporating user feedback could improve segmentation tools, enhancing their practicality.
- (vi) *Real-Time Segmentation* - Many applications, viz. robotics and autonomous vehicles, require real-time segmentation. Optimizing SSL segmentation models would expand their applicability in time-sensitive environments.

VI. CONCLUSION

This study investigates recent developments in self-supervised learning for image segmentation. While supervised learning remains the standard, its dependence on large annotated datasets has increased interest in self-supervised learning as an efficient alternative. By categorizing pretext tasks and examining dataset sources, this work comprehensively analyzes self-supervised learning's potential across various domains.

Key insights from this study include: (i) Scalability - SSL segmentation methods enable training on large datasets without manual annotation. (ii) Diverse Applications: SSL-driven segmentation extends beyond medical imaging to agriculture, robotics, and other fields. (iii) Multitasking: Integrating multiple pretext tasks enhances feature learning and representation quality of the models for downstream tasks.

As SSL continues to evolve, future research should prioritize efficiency, scalability, and adaptability to complex segmentation challenges. Advancements in these areas will be crucial for maximizing the utility of unlabeled data in building robust models. Our ongoing efforts focus on refining SSL methodologies for domain-specific applications, reinforcing its role as a transformative force in machine learning.

REFERENCES

- [1] L. Zhang and Q. Ji, "Image segmentation with a unified graphical model," *IEEE Trans. on pattern Anal. and Mach. Intell.*, vol. 32, no. 8, pp. 1406–1425, 2009.

- [2] E. Küçükülahlı, P. Erdoğan, and K. Polat, "Histogram-based automatic segmentation of images," *Neural Computing and Applicati.*, vol. 27, pp. 1445–1450, 2016.
- [3] S. Minaee, Y. Boykov, F. Porikli, A. Plaza, N. Kehtarnavaz, and D. Terzopoulos, "Image segmentation using deep learning: A survey," *IEEE Trans. on Pattern Analy. and Mach. Intelli.*, vol. 44, no. 7, pp. 3523–3542, 2022.
- [4] D. Mishra, S. Chaudhury, M. Sarkar, and A. S. Soin, "Ultrasound image segmentation: a deeply supervised network with attention to boundaries," *IEEE Trans. on Biomedical Engineering*, vol. 66, no. 6, pp. 1637–1648, 2018.
- [5] S. Hao, Y. Zhou, and Y. Guo, "A brief survey on semantic segmentation with deep learning," *Neurocomputing*, vol. 406, pp. 302–321, 2020.
- [6] N. Araslanov and S. Roth, "Single-stage semantic segmentation from image labels," in *Proc. of the IEEE/CVF Conf. on Compu. Vis. and Pattern Recognit.*, pp. 4253–4262, 2020.
- [7] J. Chen, J. Lu, X. Zhu, and L. Zhang, "Generative semantic segmentation," in *Proc. of the IEEE/CVF Conf. on Compu. Vis. and Pattern Recognit. (CVPR)*, pp. 7111–7120, June 2023.
- [8] J. Novosel, P. Viswanath, and B. Arsenali, "Boosting semantic segmentation with multi-task self-supervised learning for autonomous driving applicati.," in *Proc. of NeurIPS-Workshops*, vol. 3, 2019.
- [9] A. Kalapos and B. Gyires-Tóth, "Self-supervised pretraining for 2d medical image segmentation," in *Compu. Vis.–ECCV 2022 Workshops: Tel Aviv, Israel, Proc., Part VII*, pp. 472–484, Springer, 2023.
- [10] A. Valada, R. Mohan, and W. Burgard, "Self-supervised model adaptation for multimodal semantic segmentation," *Intl. Journal of Compu. Vis.*, vol. 128, no. 5, pp. 1239–1285, 2020.
- [11] D. Mahapatra, A. Poellinger, L. Shao, and M. Reyes, "Interpretability-driven sample selection using self supervised learning for disease classification and segmentation," *IEEE Trans. on medical imaging*, vol. 40, no. 10, pp. 2548–2562, 2021.
- [12] N. Jahan, T. Akilan, and T. M. Nguyen, "Improved semi-supervised attention gan for semantic segmentation," in *2024 IEEE Pacific Rim Conf. on Communications, Computers and Sig. Process. (PACRIM)*, pp. 1–6, 2024.
- [13] A. Kirillov, K. He, R. Girshick, and P. Dollár, "A unified architecture for instance and semantic segmentation," in *Compu. Vis. and Pattern Recognit. Conf., CVPR*, 2017.
- [14] Y. Liu and S. Gould, "Unsupervised dense prediction using differentiable normalized cuts," in *ECCV*, pp. 287–304, Springer, 2025.
- [15] J. Gui, T. Chen, J. Zhang, Q. Cao, Z. Sun, H. Luo, and D. Tao, "A survey on self-supervised learning: Algorithms, applicati., and future trends," *IEEE Trans. on Pattern Analy. and Mach. Intelli.*, 2024.
- [16] C. You, W. Dai, F. Liu, Y. Min, N. C. Dvornek, X. Li, D. A. Clifton, L. Staib, and J. S. Duncan, "Mine your own anatomy: Revisiting medical image segmentation with extremely limited labels," *IEEE Trans. on Pattern Analy. and Mach. Intelli.*, vol. 46, no. 12, pp. 11136–11151, 2024.
- [17] I. Misra and L. v. d. Maaten, "Self-supervised learning of pretext-invariant representations," in *Proc. of the IEEE/CVF Conf. on Compu. Vis. and Pattern Recognit.*, pp. 6707–6717, 2020.
- [18] E. Wallin, L. Svensson, F. Kahl, and L. Hammarstrand, "Improving open-set semi-supervised learning with self-supervision," in *Proc. of the IEEE/CVF Winter Conf. on Applicati. of Compu. Vis.*, pp. 2356–2365, 2024.
- [19] M. Caron, N. Houlsby, and C. Schmid, "Location-aware self-supervised transformers for semantic segmentation," in *Proc. of the IEEE/CVF Winter Conf. on Applicati. of Compu. Vis.*, pp. 117–127, 2024.
- [20] X. Zhai, A. Oliver, A. Kolesnikov, and L. Beyer, "S4L: Self-supervised semi-supervised learning," in *Proc. of the IEEE/CVF Intl. Conf. on Compu. Vis.*, pp. 1476–1485, 2019.
- [21] T. Afouras, A. Owens, J. S. Chung, and A. Zisserman, "Self-supervised learning of audio-visual objects from video," in *Compu. Vis.–ECCV 2020: 16th European Conf., Glasgow, UK, August 23–28, 2020, Proc., Part XVIII 16*, pp. 208–224, Springer, 2020.
- [22] S. Azizi, B. Mustafa, F. Ryan, Z. Beaver, J. Freyberg, J. Deaton, A. Loh, A. Karthikesalingam, S. Kornblith, T. Chen, et al., "Big self-supervised models advance medical image classification," in *Proc. of the IEEE/CVF Intl. Conf. on Compu. Vis.*, pp. 3478–3488, 2021.
- [23] F. Wang, T. Kong, R. Zhang, H. Liu, and H. Li, "Self-supervised learning by estimating twin class distribution," *IEEE Trans. on Image Process.*, 2023.
- [24] H. Sowrirajan, J. Yang, A. Y. Ng, and P. Rajpurkar, "Moco pretraining improves representation and transferability of chest x-ray models," in *Medical Imaging with Deep Learning*, pp. 728–744, PMLR, 2021.
- [25] X. Li, X. Hu, X. Qi, L. Yu, W. Zhao, P.-A. Heng, and L. Xing, "Rotation-oriented collaborative self-supervised learning for retinal disease diagnosis," *IEEE Trans. on Medical Imaging*, vol. 40, no. 9, pp. 2284–2294, 2021.
- [26] Y. Xie, J. Zhang, Z. Liao, Y. Xia, and C. Shen, "Pgl: prior-guided local self-supervised learning for 3d medical image segmentation," *arXiv:2011.12640*, 2020.
- [27] A. S. Xu, N. I. Shamsi, L. A. Gjestebj, and L. J. Brattain, "Self-supervised edge detection reconstruction for topology-informed 3d axon segmentation and centerline detection," in *Proc. of the IEEE/CVF Winter Conf. on Applicati. of Compu. Vis.*, pp. 7831–7839, 2024.
- [28] Q.-S. Zhu, J. Zhang, Z.-Q. Zhang, and L.-R. Dai, "A joint speech enhancement and self-supervised representation learning framework for noise-robust speech recognition," *IEEE/ACM Trans. on Audio, Speech, and Language Process.*, 2023.
- [29] Z. Lan, M. Chen, S. Goodman, K. Gimpel, P. Sharma, and R. Soicrut, "Albert: A lite bert for self-supervised learning of language representations," in *Intl. Conf. on Learning Representations*, 2019.
- [30] L. Jing and Y. Tian, "Self-supervised visual feature learning with deep neural networks: A survey," *IEEE Trans. on pattern Analy. and Mach. Intelli.*, vol. 43, no. 11, pp. 4037–4058, 2021.
- [31] K. Ohri and M. Kumar, "Review on self-supervised image recogni. using deep neural networks," *Knowledge-Based Systems*, vol. 224, p. 107090, 2021.
- [32] J. Xu, "A review of self-supervised learning methods in the field of medical image analy.," *Intl. Journal of Image, Graphics and Sig. Process. (IJIGSP)*, vol. 13, no. 4, pp. 33–46, 2021.
- [33] S. Shurrah and R. Duwairi, "Self-supervised learning methods and applicati. in medical imaging analysis: A survey," *PeerJ Computer Science*, vol. 8, p. e1045, 2022.
- [34] S. Albelwi, "Survey on self-supervised learning: auxiliary pretext tasks and contrastive learning methods in imaging," *Entropy*, vol. 24, no. 4, p. 551, 2022.
- [35] C. Chen, C. Qin, H. Qiu, G. Tarroni, J. Duan, W. Bai, and D. Rueckert, "Deep learning for cardiac image segmentation: a review," *Frontiers in Cardiovascular Medicine*, vol. 7, p. 25, 2020.
- [36] Z. Liu, L. Tong, L. Chen, Z. Jiang, F. Zhou, Q. Zhang, X. Zhang, Y. Jin, and H. Zhou, "Deep learning based brain tumor segmentation: a survey," *Complex & intelli. sys.*, vol. 9, no. 1, pp. 1001–1026, 2023.
- [37] G. Huang, I. Laradji, D. Vazquez, S. Lacoste-Julien, and P. Rodriguez, "A survey of self-supervised and few-shot object detection," *IEEE Trans. on Pattern Analy. and Mach. Intelli.*, 2022.
- [38] Y. Wang, C. M. Albrecht, N. A. A. Braham, L. Mou, and X. X. Zhu, "Self-supervised learning in remote sensing: A review," *arXiv:2206.13188*, 2022.
- [39] V. Rani, S. T. Nabi, M. Kumar, A. Mittal, and K. Kumar, "Self-supervised learning: A succinct review," *Archives of Computational Methods in Engineering*, pp. 1–15, 2023.
- [40] M.-E. Nilsback and A. Zisserman, "A visual vocabulary for flower classification," in *Proc. of the IEEE Conf. on Compu. Vis. and Pattern Recognit. (CVPR)*, 2006.
- [41] B. Zhou, H. Zhao, X. Puig, S. Fidler, A. Barriuso, and A. Torralba, "Scene parsing through ade20k dataset," in *Proc. of the IEEE Conf. on Compu. Vis. and Pattern Recognit.*, pp. 633–641, 2017.
- [42] H. Freeman and L. Garder, "Apictorial jigsaw puzzles: The computer solution of a problem in pattern recognition," *IEEE Trans. on Electronic Computers*, no. 2, pp. 118–127, 1964.
- [43] S. Gidaris, P. Singh, and N. Komodakis, "Unsupervised representation learning by predicting image rotations," in *Intl. Conf. on Learning Representations*, 2018.
- [44] Y. Li, T. Luan, Y. Wu, S. Pan, Y. Chen, and X. Yang, "Anatomask: Enhancing medical image segmentation with reconstruction-guided self-masking," in *ECCV*, pp. 146–163, Springer, 2025.
- [45] D. Pathak, P. Krahenbuhl, J. Donahue, T. Darrell, and A. A. Efros, "Context encoders: Feature learning by inpainting," in *Proc. of the IEEE Conf. on Compu. Vis. and Patt. Recognit.*, pp. 2536–2544, 2016.
- [46] M.-I. Georgescu, A. Barbalau, R. T. Ionescu, F. S. Khan, M. Popescu, and M. Shah, "Anomaly detection in video via self-supervised and multi-task learning," in *Proc. of the IEEE/CVF Conf. on Compu. Vis. and Pattern Recognit.*, pp. 12742–12752, 2021.
- [47] N. Dong, M. Kampffmeyer, and I. Voiculescu, "Self-supervised multi-task representation learning for sequential medical images," in *Machine Learning and Knowledge Discovery in Databases. Research Track*, vol. 12977, pp. 779–794, Springer Intl. Publishing, 2021.
- [48] A. Mohamed, H.-y. Lee, L. Borgholt, J. D. Havtorn, J. Edin, C. Igel, K. Kirchhoff, S.-W. Li, K. Livescu, L. Maaløe, et al., "Self-supervised

- speech representation learning: A review,” *IEEE Journal of Selected Topics in Sig. Process.*, vol. 16, no. 6, pp. 1179–1210, 2022.
- [49] Y. Xie, Z. Wang, and S. Ji, “Noise2same: Optimizing a self-supervised bound for image denoising,” *Advan. in Neural info. process. sys.*, vol. 33, pp. 20320–20330, 2020.
- [50] B. Kazimi, K. Ruzaveva, and S. Sandfeld, “Self-supervised learning with generative adversarial networks for electron microscopy,” in *Proc. of IEEE/CVF Conf. on Compu. Vis. & Patt. Recognit.*, pp. 71–81, 2024.
- [51] J. Xu, L. Xiao, and A. M. López, “Self-supervised domain adaptation for computer vision tasks,” *IEEE Access*, vol. 7, pp. 156694–156706, 2019.
- [52] W. Liao, Q. Wang, X. Li, Y. Liu, Z. Chen, S. Huang, D. Dou, Y. Xu, and H. Xiong, “Mtpret: Improving x-ray image analytics with multitask pretraining,” *IEEE Trans. on Artificial Intelli.*, vol. 5, no. 9, pp. 4799–4812, 2024.
- [53] C. Shi, C. Sun, Y. Wu, and Y. Jia, “Video anomaly detection via sequentially learning multiple pretext tasks,” in *Proc. of the IEEE/CVF Intl. Conf. on Compu. Vis.*, pp. 10330–10340, 2023.
- [54] K. Kotar, G. Ilharco, L. Schmidt, K. Ehsani, and R. Mottaghi, “Contrasting contrastive self-supervised representation learning pipelines,” in *Proc. of the IEEE/CVF Intl. Conf. on Compu. Vis.*, pp. 9949–9959, 2021.
- [55] A. Kirillov, K. He, R. Girshick, C. Rother, and P. Dollár, “Panoptic segmentation,” in *Proc. of the IEEE/CVF Conf. on Compu. Vis. and Pattern Recognit.*, pp. 9404–9413, 2019.
- [56] Y. Li, H. Qi, J. Dai, X. Ji, and Y. Wei, “Fully convolutional instance-aware semantic segmentation,” in *Proc. of the IEEE Conf. on Compu. Vis. and Pattern Recognit.*, pp. 2359–2367, 2017.
- [57] Q. Yang, J. Peng, and D. Chen, “A review of research on instance segmentation based on deep learning,” in *Intl. Conf. on Computer Engineering and Networks*, pp. 43–53, Springer, 2023.
- [58] X. Ma, X. Zhang, M.-O. Pun, and M. Liu, “A multilevel multimodal fusion transformer for remote sensing semantic segmentation,” *IEEE Trans. on Geoscience and Remote Sensing*, vol. 62, pp. 1–15, 2024.
- [59] Q. Zhou, L. Wang, G. Gao, B. Kang, W. Ou, and H. Lu, “Boundary-guided lightweight semantic segmentation with multi-scale semantic context,” *IEEE Trans. on Multimedia*, vol. 26, pp. 7887–7900, 2024.
- [60] G. J. Brostow, J. Fauqueur, and R. Cipolla, “Semantic object classes in video: A high-definition ground truth database,” *Pattern recognition letters*, vol. 30, no. 2, pp. 88–97, 2009.
- [61] Y. Yin, H. Chen, W. Zhou, J. Deng, H. Xu, and H. Li, “Revisiting open-set panoptic segmentation,” *Proc. of the AAAI Conf. on Artificial Intelli.*, vol. 38, no. 7, pp. 6747–6754, 2024.
- [62] F. Hong, L. Kong, H. Zhou, X. Zhu, H. Li, and Z. Liu, “Unified 3d and 4d panoptic segmentation via dynamic shifting networks,” *IEEE Transactions on Pattern Analysis and Machine Intelligence*, vol. 46, no. 5, pp. 3480–3495, 2024.
- [63] J. Hu, L. Huang, T. Ren, S. Zhang, R. Ji, and L. Cao, “You only segment once: Towards real-time panoptic segmentation,” in *Proc. of the IEEE/CVF Conf. on Compu. Vis. and Pattern Recognit.*, pp. 17819–17829, 2023.
- [64] V. Marsocci, S. Scardapane, and N. Komodakis, “Mare: Self-supervised multi-attention resu-net for semantic segmentation in remote sensing,” *Remote Sensing*, vol. 13, no. 16, p. 3275, 2021.
- [65] S. Chen, G. Bortsova, A. García-Uceda Juárez, G. Van Tulder, and M. De Bruijne, “Multi-task attention-based semi-supervised learning for medical image segmentation,” in *Medical Image Computing and Compu. Assis. Intervent.-MICCAI 2019: 22nd Intl. Conf., Shenzhen, China, Proc., Part III 22*, pp. 457–465, Springer, 2019.
- [66] X. Zhang, W. Xie, C. Huang, Y. Zhang, X. Chen, Q. Tian, and Y. Wang, “Self-supervised tumor segmentation with sim2real adaptation,” *IEEE Journal of Biomedical and Health Informatics*, 2023.
- [67] X. Zhang, W. Xie, C. Huang, Y. Wang, Y. Zhang, X. Chen, and Q. Tian, “Self-supervised tumor segmentation through layer decomposition,” *arXiv:2109.03230*, 2021.
- [68] L.-C. Chen, G. Papandreou, I. Kokkinos, K. Murphy, and A. L. Yuille, “Deeplab: Semantic image segmentation with deep convolutional nets, atrous convolution, and fully connected crfs,” *IEEE Trans. on Pattern Analy. and Mach. Intelli.*, vol. 40, no. 4, pp. 834–848, 2018.
- [69] D. Patel, D. Patel, R. Saxena, and T. Akilan, “Multi-class brain tumor segmentation using graph attention network,” in *2023 8th Intl. Conf. on Signal and Image Process. (ICSIP)*, pp. 196–201, IEEE, 2023.
- [70] A. Dosovitskiy, J. T. Springenberg, M. Riedmiller, and T. Brox, “Discriminative unsupervised feature learning with convolutional neural networks,” in *Advan. in Neural info. process. sys. (Z. Ghahramani, M. Welling, C. Cortes, N. Lawrence, and K. Weinberger, eds.)*, vol. 27, Curran Associates, Inc., 2014.
- [71] R. Guldenering and L. Nalpanitidis, “Self-supervised contrastive learning on agricultural images,” *Computers and Electronics in Agriculture*, vol. 191, p. 106510, 2021.
- [72] R. Zhao, Y. Zhu, and Y. Li, “Cla: A self-supervised contrastive learning method for leaf disease identification with domain adaptation,” *Computers and Electronics in Agriculture*, vol. 211, p. 107967, 2023.
- [73] X. Chen and K. He, “Exploring simple siamese representation learning,” in *Proc. of the IEEE/CVF Conf. on Compu. Vis. and Pattern Recognit.*, pp. 15750–15758, 2021.
- [74] A. Siddique, A. Tabb, and H. Medeiros, “Self-supervised learning for panoptic segmentation of multiple fruit flower species,” *IEEE Robotics and Automation Letters*, vol. 7, no. 4, pp. 12387–12394, 2022.
- [75] N. Araslanov and S. Roth, “Self-supervised augmentation consistency for adapting semantic segmentation,” in *Proc. of the IEEE/CVF Conf. on Compu. Vis. and Pattern Recognit.*, pp. 15384–15394, 2021.
- [76] W. Li, H. Chen, and Z. Shi, “Semantic segmentation of remote sensing images with self-supervised multitask representation learning,” *IEEE Journal of Selected Topics in Applied Earth Observations and Remote Sensing*, vol. 14, pp. 6438–6450, 2021.
- [77] Y. Ye, J. Zhang, Z. Chen, and Y. Xia, “Cads: A self-supervised learner via cross-modal alignment and deep self-distillation for ct volume segmentation,” *IEEE Trans. on Medical Imaging*, 2024.
- [78] M. Noroozi and P. Favaro, “Unsupervised learning of visual representations by solving jigsaw puzzles,” in *ECCV*, pp. 69–84, Springer, 2016.
- [79] Z. Yang, H. Yu, Y. He, W. Sun, Z.-H. Mao, and A. Mian, “Fully convolutional network-based self-supervised learning for semantic segmentation,” *IEEE Trans. on Neural Networks and Learn. Sys.*, 2022.
- [80] A. Taleb, C. Lippert, T. Klein, and M. Nabi, “Multimodal self-supervised learning for medical image analy.,” in *Informa. Process. in Medical Imaging: 27th Intl. Conf., IPMI 2021, Virtual Event, June 28–June 30, 2021, Proceedings*, pp. 661–673, Springer, 2021.
- [81] J. Ni, Z. Wang, Y. Wang, W. Tao, and A. Shen, “Drcl: rethinking jigsaw puzzles for unsupervised medical image segmentation,” *The Visual Computer*, pp. 1–15, 2024.
- [82] Z. Song, Z. Hu, and R. Hong, “Grid feature jigsaw for self-supervised image clustering,” in *2023 Intl. Joint Conf. on Neural Networks (IJCNN)*, pp. 1–7, IEEE, 2023.
- [83] G. Wang, Y. Wang, J. Qin, D. Zhang, X. Bao, and D. Huang, “Video anomaly detection by solving decoupled spatio-temporal jigsaw puzzles,” in *ECCV*, pp. 494–511, Springer, 2022.
- [84] W. Park and J. Ryu, “Fine-grained self-supervised learning with jigsaw puzzles for medical image classification,” *Computers in Biology and Medicine*, vol. 174, p. 108460, 2024.
- [85] Y. Yu, S. Shin, M. Ko, and K. Lee, “Exploring using jigsaw puzzles for out-of-distribution detection,” *Compu. Vis. and Image Understanding*, vol. 241, p. 103968, 2024.
- [86] S. Markaki and C. Panagiotakis, “Jigsaw puzzle solving techniques and applicati.: a survey,” *The Visual Computer*, vol. 39, no. 10, pp. 4405–4421, 2023.
- [87] A. G. Bromley, “Charles babbage’s analytical engine, 1838,” *Annals of the History of Computing*, vol. 4, no. 3, pp. 196–217, 1982.
- [88] D. Zhukov, J.-B. Alayrac, I. Laptev, and J. Sivic, “Learning actionness via long-range temporal order verification,” in *Compu. Vis.-ECCV 2020: 16th European Conf., Glasgow, UK, August 23–28, 2020, Proc., Part XXIX 16*, pp. 470–487, Springer, 2020.
- [89] I. Misra, C. L. Zitnick, and M. Hebert, “Shuffle and learn: unsupervised learning using temporal order verification,” in *Compu. Vis.-ECCV 2016: 14th European Conf., Amsterdam, The Netherlands, Proc., Part I 14*, pp. 527–544, Springer, 2016.
- [90] P. Zhang, F. Wang, and Y. Zheng, “Self supervised deep representation learning for fine-grained body part recognition,” in *2017 IEEE 14th intl. sympos. on biomedical imaging*, pp. 578–582, IEEE, 2017.
- [91] N. Shvetsova, F. Petersen, A. Kukleva, B. Schiele, and H. Kuehne, “Learning by sorting: Self-supervised learning with group ordering constraints,” in *Proc. of the IEEE/CVF Intl. Conf. on Compu. Vis.*, pp. 16453–16463, 2023.
- [92] C. Yang, W. Xie, and A. Zisserman, “Made to order: Discovering monotonic temporal changes via self-supervised video ordering,” *arXiv:2404.16828*, 2024.
- [93] D. Jayaraman and K. Grauman, “Slow and steady feature analysis: higher order temporal coherence in video,” in *Proc. of the IEEE Conf. on Compu. Vis. and Pattern Recognit.*, pp. 3852–3861, 2016.
- [94] N. Srivastava, E. Mansimov, and R. Salakhudinov, “Unsupervised learning of video representations using lstms,” in *Intl. Conf. on machine learning*, pp. 843–852, PMLR, 2015.

- [95] H. Spitzer, K. Kiwitz, K. Amunts, S. Harmeling, and T. Dickscheid, "Improving cytoarchitectonic segmentation of human brain areas with self-supervised siamese networks," in *Medical Image Computing and Compu. Assis. Intervent.-MICCAI 2018: 21st Intl. Conf., Granada, Spain, Proc., Part III 11*, pp. 663–671, Springer, 2018.
- [96] J. Wang, B. Hu, Y. Long, and Y. Guan, "Order matters: Shuffling sequence generation for video prediction," in *30th British Machine Vision Conf. 2019, BMVC 2019*, Newcastle University, 2020.
- [97] Z. Feng, C. Xu, and D. Tao, "Self-supervised representation learning by rotation feature decoupling," in *Proc. of the IEEE/CVF Conf. on Compu. Vis. and Pattern Recognit.*, pp. 10364–10374, 2019.
- [98] W. Deng, S. Gould, and L. Zheng, "What does rotation prediction tell us about classifier accuracy under varying testing environments?," in *Intl. Conf. on Machine Learning*, pp. 2579–2589, PMLR, 2021.
- [99] J. Linmans, J. Winkens, B. S. Veeling, T. S. Cohen, and M. Welling, "Sample efficient semantic segmentation using rotation equivariant convolutional networks," *arXiv:1807.00583*, 2018.
- [100] X. Zhuang, Y. Li, Y. Hu, K. Ma, Y. Yang, and Y. Zheng, "Self-supervised feature learning for 3d medical images by playing a rubik's cube," in *Medical Image Computing and Compu. Assis. Intervent.-MICCAI 2019: 22nd Intl. Conf., Shenzhen, China, Proc., Part IV 22*, pp. 420–428, Springer, 2019.
- [101] J. Zhu, Y. Li, Y. Hu, K. Ma, S. K. Zhou, and Y. Zheng, "Rubik's cube+: A self-supervised feature learning framework for 3d medical image analy.," *Medical image analy.*, vol. 64, p. 101746, 2020.
- [102] X. Tao, Y. Li, W. Zhou, K. Ma, and Y. Zheng, "Revisiting rubik's cube: Self-supervised learning with volume-wise transformation for 3d medical image segmentation," in *Medical Image Computing and Compu. Assis. Intervent.-MICCAI 2020: 23rd Intl. Conf., Lima, Peru, Proc., Part IV 23*, pp. 238–248, Springer, 2020.
- [103] H. J. Kuijff, E. Bennink, K. L. Vincken, N. Weaver, G. J. Biessels, and M. A. Viergever, "MR Brain Segmentation Challenge 2018 Data," 2024.
- [104] X. Liu, F. Zhang, Z. Hou, L. Mian, Z. Wang, J. Zhang, and J. Tang, "Self-supervised learning: Generative or contrastive," *IEEE Trans. on knowledge and data engineering*, vol. 35, no. 1, pp. 857–876, 2021.
- [105] M. Soliman, C. Lehman, and G. AlRegib, "S6: semi-supervised self-supervised semantic segmentation," in *IEEE Intl. Conf. on Image Process. (ICIP)*, pp. 1861–1865, IEEE, 2020.
- [106] Z. Zeng, Y. Xulei, Y. Qiyun, Y. Meng, and Z. Le, "Sese-net: Self-supervised deep learning for segmentation," *Pattern Recogni. Letters*, vol. 128, pp. 23–29, 2019.
- [107] B. Felfelyan, N. D. Forkert, A. Hareendranathan, D. Cornel, Y. Zhou, G. Kuntze, J. L. Jaremkó, and J. L. Ronsky, "Self-supervised-rcnn for medical image segmentation with limited data annotation," *Computerized Medical Imaging and Graphics*, vol. 109, p. 102297, 2023.
- [108] F.-A. Croitoru, V. Hondru, R. T. Ionescu, and M. Shah, "Diffusion models in vision: A survey," *IEEE Trans. on Pattern Analy. and Mach. Intelli.*, vol. 45, no. 9, pp. 10850–10869, 2023.
- [109] J. Li, M. Gong, W. Li, M. Zhang, Y. Zhang, S. Wang, and Y. Wu, "Ms 2 a 2 net: Multi-scale self-attention aggregation network for few-shot aerial imagery segmentation," *IEEE Trans. on Geoscience and Remote Sensing*, 2023.
- [110] S. Treneska, E. Zdravetski, I. M. Pires, P. Lameski, and S. Gievaska, "Gan-based image colorization for self-supervised visual feature learning," *Sensors*, vol. 22, no. 4, p. 1599, 2022.
- [111] I. Žeger, S. Grgic, J. Vuković, and G. Šišul, "Grayscale image colorization methods: Overview and evaluation," *IEEE access*, vol. 9, pp. 113326–113346, 2021.
- [112] J. González-Santiago, F. Schenkel, and W. Middelman, "Self-supervised image colorization for semantic segmentation of urban land cover," in *2021 IEEE Intl. Geoscience and Remote Sensing Symposium IGARSS*, pp. 3468–3471, IEEE, 2021.
- [113] H. Chen, "Color-s⁴l: Self-supervised semi-supervised learning with image colorization," *arXiv:2401.03753*, 2024.
- [114] R. Zhang, P. Isola, and A. A. Efros, "Colorful image colorization," in *Compu. Vis.-ECCV 2016: 14th European Conf., Amsterdam, The Netherlands, Proc., Part III 14*, pp. 649–666, Springer, 2016.
- [115] G. Larsson, M. Maire, and G. Shakhnarovich, "Learning representations for automatic colorization," in *Compu. Vis.-ECCV 2016: 14th European Conf., Amsterdam, The Netherlands, Proc., Part IV 14*, pp. 577–593, Springer, 2016.
- [116] X. Lin, C. Li, S. Adams, A. Kouzani, R. Jiang, L. He, Y. Hu, M. Vernon, E. Döven, L. Webb, et al., "Self-supervised leaf segmentation under complex lighting conditions," *Pattern Recognition*, vol. 135, p. 109021, 2023.
- [117] M.-Y. Ho, C.-M. Wu, M.-S. Wu, and Y. J. Tseng, "Every pixel has its moments: Ultra-high-resolution unpaired image-to-image translation via dense normalization," in *ECCV*, pp. 312–328, Springer, 2025.
- [118] H.-J. Kim and D. Lee, "Image denoising with conditional generative adversarial networks (cgan) in low dose chest images," *Nuclear Instruments and Methods in Physics Research Section A: Accelerators, Spectromet., Detect. & Associa. Equipm.*, vol. 954, p. 161914, 2020.
- [119] I. Goodfellow, J. Pouget-Abadie, M. Mirza, B. Xu, D. Warde-Farley, S. Ozair, A. Courville, and Y. Bengio, "Generative adversarial nets," *Advan. in neural info. process. sys.*, vol. 27, 2014.
- [120] P. Luc, C. Couprie, S. Chintala, and J. Verbeek, "Semantic segmentation using adversarial networks," in *NIPS Workshop on Adversarial Training*, 2016.
- [121] W. C. Hung, Y. H. Tsai, Y. T. Liou, Y.-Y. Lin, and M. H. Yang, "Adversarial learning for semi-supervised semantic segmentation," in *29th British Machine Vision Conf., BMVC 2018*, 2018.
- [122] V. Belagali, S. Yellapragada, A. Graikos, S. Kapse, Z. Li, T. N. Nandi, R. K. Madduri, P. Prasanna, J. Saltz, and D. Samaras, "Genesis: Generative self-augmentation improves self-supervised learning," *arXiv:2412.01672*, 2024.
- [123] D. Li, J. Yang, K. Kreis, A. Torralba, and S. Fidler, "Semantic segmentation with generative models: Semi-supervised learning and strong out-of-domain generalization," in *Proc. of the IEEE/CVF Conf. on Compu. Vis. and Pattern Recognit.*, pp. 8300–8311, 2021.
- [124] M. Prakash, T.-O. Buchholz, M. Lalit, P. Tomancak, F. Jug, and A. Krull, "Leveraging self-supervised denoising for image segmentation," in *2020 IEEE 17th intl. sympos. on biomedical imaging (ISBI)*, pp. 428–432, IEEE, 2020.
- [125] N. Martinez, G. Sapiro, A. Tannenbaum, T. J. Hollmann, and S. Nadeem, "Impartial: Partial annotations for cell instance segmentation," *bioRxiv*, pp. 2021–01, 2021.
- [126] J. Zhang, Y. Liu, C. Guo, and J. Zhan, "Optimized segmentation with image inpainting for semantic mapping in dynamic scenes," *Applied Intelli.*, vol. 53, no. 2, pp. 2173–2188, 2023.
- [127] S. He, Q. Li, Y. Liu, and W. Wang, "Semantic segmentation of remote sensing images with self-supervised semantic-aware inpainting," *IEEE Geoscience and Remote Sensing Letters*, vol. 19, pp. 1–5, 2022.
- [128] I. Katircioglu, H. Rhodin, V. Constantin, J. Spörri, M. Salzmann, and P. Fua, "Self-supervised segmentation via background inpainting," *arXiv:2011.05626*, 2020.
- [129] M. Caron, N. Houlsby, and C. Schmid, "Location-aware self-supervised transformers for semantic segmentation," in *Proc. of the IEEE/CVF Winter Conference on Applications of Compu. Vis.*, pp. 117–127, 2024.
- [130] F. Pan, I. Shin, F. Rameau, S. Lee, and I. S. Kweon, "Unsupervised intra-domain adaptation for semantic segmentation through self-supervision," in *Proc. of the IEEE/CVF Conf. on Compu. Vis. and Pattern Recognit.*, pp. 3764–3773, 2020.
- [131] D. Wu, J. Cheng, Z. Li, and Z. Chen, "Image inpainting based on fusion structure information and pixelwise attention," *The Visual Computer*, pp. 1–17, 2024.
- [132] L. Chen, P. Bentley, K. Mori, K. Misawa, M. Fujiwara, and D. Rueckert, "Self-supervised learning for medical image analysis using image context restoration," *Medical image analy.*, vol. 58, p. 101539, 2019.
- [133] W. Li, H. Chen, and Z. Shi, "Semantic segmentation of remote sensing images with self-supervised multitask representation learning," *IEEE Journal of Selected Topics in Applied Earth Observations and Remote Sensing*, vol. 14, pp. 6438–6450, 2021.
- [134] J.-B. Grill, F. Strub, F. Altché, C. Tallec, P. Richemond, E. Buchatskaya, C. Doersch, B. Avila Pires, Z. Guo, M. Gheshlaghi Azar, et al., "Bootstrap your own latent-a new approach to self-supervised learning," *Advan. in neural info. process. sys.*, vol. 33, pp. 21271–21284, 2020.
- [135] D. Hjelm, A. Fedorov, S. Lavoie-Marchildon, K. Grewal, P. Bachman, A. Trischler, and Y. Bengio, "Learning deep representations by mutual information estimation and maximization," ICLR, April 2019.
- [136] T. Chen, S. Kornblith, M. Norouzi, and G. Hinton, "A simple framework for contrastive learning of visual representations," in *Intl. Conf. on machine learning*, pp. 1597–1607, PMLR, 2020.
- [137] K. He, H. Fan, Y. Wu, S. Xie, and R. Girshick, "Momentum contrast for unsupervised visual representation learning," in *Proc. of the IEEE/CVF Conf. on Compu. Vis. and Pattern Recognit.*, pp. 9729–9738, 2020.
- [138] D.-Y. She and K. Xu, "Contrastive self-supervised representation learning using synthetic data," *Intl. Journal of Automation and Computing*, vol. 18, no. 4, pp. 556–567, 2021.
- [139] S. Karimijafarbigloo, R. Azad, A. Kazerouni, Y. Velichko, U. Bagci, and D. Merhof, "Self-supervised semantic segmentation: Consistency over transformation," in *Proc. of the IEEE/CVF Intl. Conf. on Compu. Vis.*, pp. 2654–2663, 2023.

- [140] A. v. d. Oord, Y. Li, and O. Vinyals, "Representation learning with contrastive predictive coding," *arXiv:1807.03748*, 2018.
- [141] O. Henaff, "Data-efficient image recogni. with contrastive predictive coding," in *Intl. Conf. on machine learning*, pp. 4182–4192, PMLR, 2020.
- [142] X. Wang, R. Zhang, C. Shen, T. Kong, and L. Li, "Dense contrastive learning for self-supervised visual pre-training," in *Proc. of the IEEE/CVF Conf. on Compu. Vis. and Pattern Recognit.*, pp. 3024–3033, 2021.
- [143] H. Hu, J. Cui, and L. Wang, "Region-aware contrastive learning for semantic segmentation," in *Proc. of the IEEE/CVF Intl. Conf. on Compu. Vis.*, pp. 16291–16301, 2021.
- [144] M. Cordts, M. Omran, S. Ramos, T. Rehfeld, M. Enzweiler, R. Benenson, U. Franke, S. Roth, and B. Schiele, "The cityscapes dataset for semantic urban scene understanding," in *Proc. of the IEEE Conf. on Compu. Vis. and Pattern Recognit.*, pp. 3213–3223, 2016.
- [145] Z. Xie, Y. Lin, Z. Yao, Z. Zhang, Q. Dai, Y. Cao, and H. Hu, "Self-supervised learning with swin transformers," 2021.
- [146] H. Caesar, J. Uijlings, and V. Ferrari, "Coco-stuff: Thing and stuff classes in context," in *Compu. Vis. and pattern Recogni. (CVPR), 2018 IEEE Conf. on, IEEE*, 2018.
- [147] M. Everingham, L. Van Gool, C. K. I. Williams, J. Winn, and A. Zisserman, "The PASCAL Visual Object Classes Challenge 2012 (VOC2012) Results," 2012.
- [148] J. Zhu, Y. Li, Y. Hu, and S. K. Zhou, "Embedding task knowledge into 3d neural networks via self-supervised learning," *arXiv preprint arXiv:2006.05798*, 2020.
- [149] P. Gandhi, D. S. Sisodia, and R. R. Jagat, "Self-supervised learning based land cover semantic segmentation of satellite imagery," in *2024 4th Intl. Conf. on Sustainable Expert Sys.*, pp. 1708–1714, IEEE, 2024.
- [150] D. Torpey and R. Klein, "Deepset simclr: Self-supervised deep sets for improved pathology representation learning," *arXiv:2402.15598*, 2024.
- [151] M. Tang, K. Georgiou, H. Qi, C. Champion, and M. Bosch, "Semantic segmentation in aerial imagery using multi-level contrastive learning with local consistency," in *Proc. of the IEEE/CVF Winter Conf. on Applicati. of Compu. Vis.*, pp. 3798–3807, 2023.
- [152] S. Landgraf, L. Kühnlein, M. Hillemann, M. Hoyer, S. Keller, and M. Ulrich, "Evaluation of self-supervised learning approaches for semantic segmentation of industrial burner flames," *The Intl. Archives of the Photogrammetry, Remote Sensing and Spatial Informa. Sci.*, vol. 43, pp. 601–607, 2022.
- [153] X. Chen, H. Fan, R. Girshick, and K. He, "Improved baselines with momentum contrastive learning," *arXiv:2003.04297*, 2020.
- [154] X. Chen, S. Xie, and K. He, "An empirical study of training self-supervised vision transformers," in *Proc. of the IEEE/CVF Intl. Conf. on Compu. Vis.*, pp. 9640–9649, 2021.
- [155] Y. Ci, C. Lin, L. Bai, and W. Ouyang, "Fast-moco: Boost momentum-based contrastive learning with combinatorial patches," in *Compu. Vis.–ECCV 2022: 17th European Conf., Tel Aviv, Israel, Proc., Part XXVI*, pp. 290–306, Springer, 2022.
- [156] Y. Wang, J. Zhang, Y. Chen, H. Yuan, and C. Wu, "An automated learning method of semantic segmentation for train autonomous driving environment understanding," *IEEE Trans. on Industr. Informat.*, 2024.
- [157] Z. Xu, Y. Dai, F. Liu, B. Wu, W. Chen, and L. Shi, "Swin moco: Improving parotid gland mri segmentation using contrastive learning," *Medical Physics*, 2024.
- [158] R. Mahmoudi Kouhi, O. Stocker, P. Giguère, and S. Daniel, "Cloudspam: Contrastive learning on unlabeled data for segmentation and pre-training using aggregated point clouds and moco," *Remote Sensing*, vol. 16, no. 21, p. 3984, 2024.
- [159] Y. Liu, S. Halek, R. Crawford, K. Persson, M. Tomaszewski, S. Wang, R. Baumgartner, J. Yuan, G. Goldmacher, and A. Chen, "3d segmentation of necrotic lung lesions in ct images using self-supervised contrastive learning," *IEEE Access*, 2024.
- [160] Z. Nisar and T. Lampert, "Maximising histopathology segmentation using minimal labels via self-supervision," *arXiv:2412.15389*, 2024.
- [161] Z. Gao and I. Patras, "Self-supervised facial representation learning with facial region awareness," in *Proc. of the IEEE/CVF Conf. on Compu. Vis. and Pattern Recognit.*, pp. 2081–2092, 2024.
- [162] X. Li, F. Xu, F. Liu, Y. Tong, X. Lyu, and J. Zhou, "Semantic segmentation of remote sensing images by interactive representation refinement and geometric prior-guided inference," *IEEE Trans. on Geoscience and Remote Sensing*, 2023.
- [163] R. Zheng, Y. Zhong, S. Yan, H. Sun, H. Shen, and K. Huang, "Msvrl: self-supervised multiscale visual representation learning via cross-level consistency for medical image segmentation," *IEEE Trans. on Medical Imaging*, vol. 42, no. 1, pp. 91–102, 2022.
- [164] Z. Tian, H. Zhao, M. Shu, Z. Yang, R. Li, and J. Jia, "Prior guided feature enrichment network for few-shot segmentation," *IEEE Transactions on Pattern Analysis and Machine Intelligence*, vol. 44, no. 2, pp. 1050–1065, 2020.
- [165] N. Heller, F. Isensee, K. H. Maier-Hein, X. Hou, C. Xie, F. Li, Y. Nan, G. Mu, Z. Lin, M. Han, et al., "The state of the art in kidney and kidney tumor segmentation in contrast-enhanced ct imaging: Results of the kits19 challenge," *Medical image analysis*, vol. 67, p. 101821, 2021.
- [166] Z. Xu, "Multi-atlas labeling beyond the cranial vault-ws and challenge," *Synapse website*, 2016.
- [167] M. Caron, I. Misra, J. Mairal, P. Goyal, P. Bojanowski, and A. Joulin, "Unsupervised learning of visual features by contrasting cluster assignments," *Advancement in neural information processing systems*, vol. 33, pp. 9912–9924, 2020.
- [168] M. Cuturi, "Sinkhorn distances: Lightspeed computation of optimal transport," *Advan. in neural info. process. sys.*, vol. 26, 2013.
- [169] M. Everingham, L. Van Gool, C. K. Williams, J. Winn, and A. Zisserman, "The pascal visual object classes (voc) challenge," *Intl. journal of Compu. Vis.*, vol. 88, pp. 303–338, 2010.
- [170] T.-Y. Lin, M. Maire, S. Belongie, J. Hays, P. Perona, D. Ramanan, P. Dollár, and C. L. Zitnick, "Microsoft coco: Common objects in context," in *Compu. Vis.–ECCV 2014: 13th European Conf., Zurich, Switzerland, Proc., Part V 13*, pp. 740–755, Springer, 2014.
- [171] Y. Zou, J. Jeong, L. Pemula, D. Zhang, and O. Dabeer, "Spot-the-difference self-supervised pre-training for anomaly detection and segmentation," in *ECCV*, pp. 392–408, Springer, 2022.
- [172] H. Wang, E. Ahn, and J. Kim, "A multi-resolution self-supervised learning framework for semantic segmentation in histopathology," *Pattern Recognition*, vol. 155, p. 110621, 2024.
- [173] T. Sakaguchi, A. Taniguchi, Y. Hagiwara, L. El Hafi, S. Hasegawa, and T. Taniguchi, "Object instance retrieval in assistive robotics: Leveraging fine-tuned simsim with multi-view images based on 3d semantic map," in *2024 IEEE/RSJ Intl. Conf. on Intelligent Robots and Sys. (IROS)*, pp. 7817–7824, IEEE, 2024.
- [174] D. Jha, P. H. Smedsrud, M. A. Riegler, D. Johansen, T. De Lange, P. Halvorsen, and H. D. Johansen, "Resunet++: An advanced architecture for medical image segmentation," in *2019 IEEE intl. sympos. on multimedia (ISM)*, pp. 225–2255, IEEE, 2019.
- [175] A. Dhamale, R. Rajalakshmi, and A. Balasundaram, "Dual multi scale networks for medical image segmentation using contrastive learning," *Image and Vision Computing*, vol. 154, p. 105371, 2025.
- [176] Z. Xie, Y. Lin, Z. Zhang, Y. Cao, S. Lin, and H. Hu, "Propagate yourself: Exploring pixel-level consistency for unsupervised visual representation learning," in *Proc. of the IEEE/CVF Conf. on Compu. Vis. and Pattern Recognit.*, pp. 16684–16693, 2021.
- [177] T. Xiao, C. J. Reed, X. Wang, K. Keutzer, and T. Darrell, "Region similarity representation learning," in *Proc. of the IEEE/CVF Intl. Conf. on Compu. Vis.*, pp. 10539–10548, 2021.
- [178] C. Yang, L. Zhang, H. Lu, X. Ruan, and M.-H. Yang, "Saliency detection via graph-based manifold ranking," in *Proc. of the IEEE Conf. on Compu. Vis. and Pattern Recognit.*, pp. 3166–3173, 2013.
- [179] W. Zhang, J. Pang, K. Chen, and C. C. Loy, "Dense siamese network for dense unsupervised learning," in *ECCV*, pp. 464–480, Springer, 2022.
- [180] K. Chaitanya, E. Erdil, N. Karani, and E. Konukoglu, "Contrastive learning of global and local features for medical image segmentation with limited annotations," *Advan. in Neural info. process. sys.*, vol. 33, pp. 12546–12558, 2020.
- [181] A. Islam, B. Lundell, H. Sawhney, S. N. Sinha, P. Morales, and R. J. Radke, "Self-supervised learning with local contrastive loss for detection and semantic segmentation," in *Proc. of the IEEE/CVF Winter Conf. on Applicati. of Compu. Vis.*, pp. 5624–5633, 2023.
- [182] N. Heller, F. Isensee, D. Trofimova, and et al., "The kits21 challenge: Automatic segmentation of kidneys, renal tumors, and renal cysts in corticomedullary-phase ct," 2023.
- [183] D. LaBella, K. Schumacher, and e. a. Mix, "Brain tumor segmentation (brats) challenge 2024: Meningioma radiotherapy planning automated segmentation," *preprint arXiv:2405.18383*, 2024.
- [184] N. Codella, V. Rotemberg, and e. a. Tschandl, "Skin lesion analysis toward melanoma detection 2018: A challenge hosted by the international skin imaging collaboration (isic)," *arXiv preprint arXiv:1902.03368*, 2019.
- [185] G. Ros, L. Sellart, J. Materzynska, D. Vazquez, and A. M. Lopez, "The synthia dataset: A large collection of synthetic images for semantic segmentation of urban scenes," in *Proc. of the IEEE Conf. on Compu. Vis. and Pattern Recognit.*, pp. 3234–3243, 2016.

- [186] M. Everingham, S. A. Eslami, L. Van Gool, C. K. Williams, J. Winn, and A. Zisserman, "The pascal visual object classes challenge: A retrospective," *Intl. journal of Compu. Vis.*, vol. 111, pp. 98–136, 2015.

VII. APPENDIX

This section provides additional details relevant to the article titled “Self-Supervised Learning for Image Segmentation: A Comprehensive Survey.”

A. Organization Mind map

Fig. 18 presents a mind map of this study.

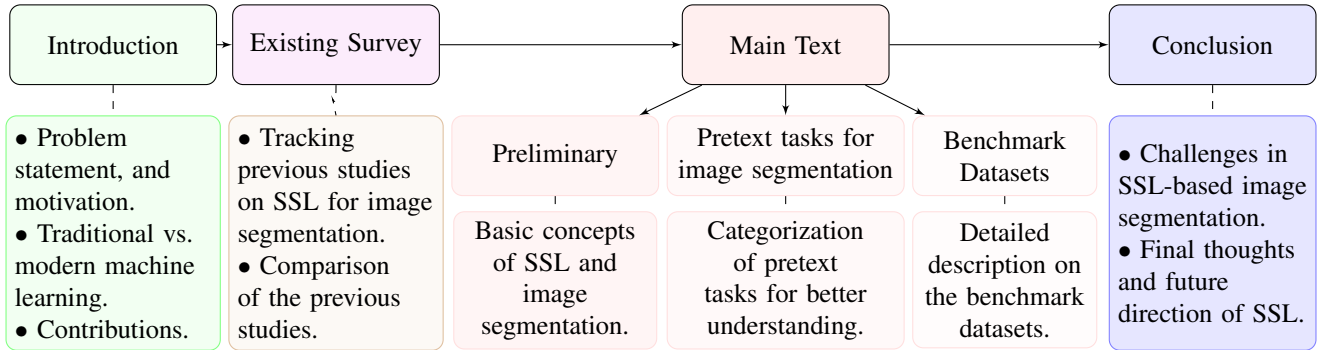


Fig. 18: The mind map of the survey.

B. Research Methodology

Fig. 19 represents the publication search and selection procedure. This study uses five widely accepted academic databases and search engines to collect peer-reviewed articles. It is observed that SSL has garnered significant attention from 2018 onwards. Thus, the selection of articles is restricted from 2018. Initially, a total of 250 articles are selected. From the selected articles, the following information is logged into a registry: *title, publication year, publication venue, data source, objectives of the study, learning type (supervised, self-supervised, or unsupervised), contributions, limitations, and challenges of the work*. By analyzing the registry and the articles’ abstract, duplicate articles and articles that do not match the scope of this survey are removed from the in-depth investigation. This study reviews over 100 articles and organizes their insights for readers. However, the total citation count in the manuscript is 186, as it includes references from other sections such as the introduction, preliminary information, and benchmark datasets.

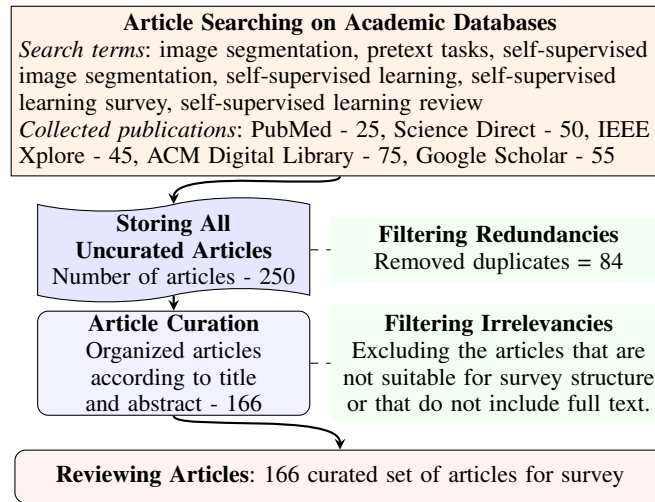


Fig. 19: The article searching and selection procedure.

C. Literature Summary

Table V on page 23 presents a concise summary of key studies from 2016 to 2025 that explore SSL for segmentation.

TABLE V: A highlight of the adaptation of self-supervised learning in different research fields. Note: \blacksquare - Segmentation using Dice score, Recall, F1-score, or IoU, \square - Object detection, and \boxtimes - Classification.

Ref.	Methodology	Pre-processing/ Pretext	Advantages	Limitations	Dataset Used	Results (%)
[78] 2016	The backbone is pre-trained solving Jigsaw puzzle. The top layers are fine-tuned to solve a downstream task, while the backbone is frozen	Creating 9-title Jigsaw puzzle permutations on ImageNet and assigning an index to each title	Learn spatial and semantic relationships within an image without labeled data	Sensitivity to tile size & grid configuration, Computationally expensive	D1: PascalVOC'07 [186]	\boxtimes D1: 67.6 \square D1: 53.2 \blacksquare D1: 37.6
[66] 2017	Layer-decomposition for generating synthetic data. A two-stage Sim2Real unsupervised self-training	Data augmentation (rotations, scaling, mirror, noise addition & blur, change in brightness)	Fine-tuning is not required, scalability	Heavily depends on the quality and realism of the synthetic data	D1: BraTS'18 [183], D2: LiTS2017	\blacksquare D1: 84.5 \blacksquare D2: 60.5
[95] 2018	Uses a self-supervised Siamese network to predict the 3D geodesic distance between image patches from histological brain sections	Extracts 1019×1019 patches from BigBrain 3D brain sections	Improves segmentation accuracy with limited labeled data	Relies on accurate 3D brain reconstruction	D1: BigBrain	\blacksquare D1: 80.0
[8] 2019	Colorization and depth prediction for semantic segmentation	Image resizing, data augmentation, depth map and grayscale generation	Claimed that depth prediction performs better than colorization	The multi-task design can lead to increased computational	D1: Cityscapes [144], D2: KITTI	\blacksquare D1: 65.0 \blacksquare D2: 49.0
[106] 2019	SeSe-Net: It uses a dual network strategy: Worker for segmentation and Supervisor for evaluating segmentation quality	Data augmentation with random shuffling to generate balanced datasets	It achieves performance improvements w/t 5% labeled data by utilizing large unlabeled data	Due to dual-network model training can be computationally intensive	D1: Carvana, D2: CMR, D3: Pet	\blacksquare D1: 76.1 \blacksquare D2: 67.9 \blacksquare D3: 69.2
[97] 2019	Decoupling the rotation-related features from task-agnostic features	Generate multiple rotated copies of the same image ($\{0^\circ, 90^\circ, 180^\circ, 270^\circ\}$) for the rotation prediction pretext	Better generalization for downstream tasks	Increased complexity, discrete rotation angles may not capture all real-world scenarios	D1: PascalVOC'07, D2: PascalVOC'12	\boxtimes D1: 74.7 \square D1: 58.0 \blacksquare D2: 45.9
[10] 2020	SSMA: a multimodal SSL model adaptation, dynamically recalibrates and fuses modality-specific features based on object class, spatial location, and scene context	Data augmentation (rotation, skewing, scaling, cropping, brightness & contrast modulation, and flipping)	Adapts feature fusion based on object class and spatial location	Requires high memory due to multi-stream architecture	D1: Cityscapes [144], D2: ScanNet, D3: SYNTHIA [185]	\blacksquare D1: 82.3 \blacksquare D2: 57.7 \blacksquare D3: 91.3
[26] 2020	PGL: A local patch-based prior-guided model	Data augmentation (flipping, cropping, and scaling)	Learn meaningful local structures	Training time is high due to model complexity	D1: KiTS [165], D2: BVC [166]	\blacksquare D1: 84.3 \blacksquare D2: 70.5
[105] 2020	An integration of supervision and self-supervision. Segmentation w/t fully-supervised fashion and reconstruction via self-supervision	An auxiliary image reconstruction task	Achieves 18% IoU improvement with only 2% labeled data	Segmentation and reconstruction loss balancing is essential for optimal performance	D1: Facies (segmented seismic images)	\blacksquare D1: 62.4
[6] 2020	A class aggregation function, a module for masking, and a stochastic gate work	Random rescaling, horizontal flipping, color jittering, and random crops	Produced high-quality semantic masks	Mislabelling and misleading under conditions of occlusions	D1: PascalVOC'12	\blacksquare D1: 64.3
[133] 2021	Pre-training a backbone jointly on multimodal (image-, patch-, and pixel-level) tasks	3 Pretext tasks (inpainting, transformation prediction, contrastive learning)	Suitable for both high-level and low-level features learning	Multiple pretext tasks increases the complexity of the training process	D1: Potsdam, D2: Vaihingen, D3: Levir_CS	\blacksquare D1: 70.7 \blacksquare D2: 74.1 \blacksquare D3: 76.5
[64] 2021	Use prediction of visual word distributions (OBoW) with attention for SSL and MAResU-Net for segmentation	Data augmentation (color jittering, gray-scaling, and Gaussian blurring)	Pretraining with OBoW allows the encoder to capture both global and local features	The combined SSL and attention-enhanced model require significant computational resources	D1: ISPRS Vaihingen	\blacksquare D1: 81.8
[67] 2021	A layer decomposition model for 3D tumor segmentation with Sim2Real synthetic data generation, and zero-shot training	Linear transformation, elastic deformation, and Gaussian blur	Disentangling tumors from the background can improve feature learning process	Computational overhead due to multi-layer processing, limited generalization	D1: BraTS'18, D2: LiTS2017	\blacksquare D1: 71.6 \blacksquare D2: 40.8
[75] 2021	SSL with momentum update to learn augmentation consistency across various augmented versions of the same image	Data augmentation (photometric noise, multi-scale fusion, and random flipping)	Achieved improvements across different backbone architectures and adaptation scenarios	Patch-size dependence, inaccurate pseudo labels can propagate errors during training	D1: Cityscapes	\blacksquare D1: 53.8
[79] 2022	A FCN patch-wise classification network trained with jigsaw puzzle proxy task for semantic segmentation	Grid-based patch generation and shuffling, Data augmentation (random mirroring and scaling)	A 5.8% improvement w/t 1/6 labeled data over a baseline model trained from scratch	The patch-wise classification increases the # of classes, complicating training	D1: PascalVOC'12	\blacksquare D1: 43.4
[107] 2023	An enhanced Mask-RCNN is pre-trained with three pretext tasks via self-supervision. The model is fine-tuned using a few labeled data	Pretext tasks: localizing the distorted area, classifying the distortion type, and recovering the distorted areas	A 20% increase in Dice score compared to models trained from scratch	Effectiveness depends on choice & relevance of used distortions to the specific context	D1: Osteoarthritis Initiative (OAI)	\blacksquare D1: 77.0
[9] 2023	Self-supervised BYOL pretraining on natural and domain-specific cardiac MRI data, followed by U-Net segmentation fine-tuning for improving accuracy	Data augmentation (random resizing and cropping, horizontal flipping, brightness, and contrast)	4 – 5 \times faster fine-tuning compared to ImageNet pretraining	Less effective in extremely low-data access	D1: Adverse Conditions Dataset w/t Correspondences (ACDC)	\blacksquare D1: 85.0
[129] 2024	LOCA (Location-Aware) SSL. Combines patch-level clustering for dense learning and relative position prediction for spatial reasoning	Pretext (position prediction, patch-level clustering), Augmentation (flipping, cropping, color jittering, etc.)	Spatially-aware robust representation learning	Balancing position prediction & patch-level clustering is crucial for optimal learning	D1: ADE20K [145], D2: Cityscapes [144], D3: CamVid [60]	\blacksquare D1: 47.9 \blacksquare D2: 79.8 \blacksquare D3: 56.1
[175] 2025	A dual multi-scale encoder-decoder network that combines EfficientNet B5 and attention-based pyramid vision transformer with Pixel-wise Contrastive Loss (PCL)	Boundary masks created using morphological operations, contrastive learning for pretext task	Integrated multi-scale analysis and PCL enables the model to capture contextually rich features	The PCL loss computation is complex, requires additional training time	D1: BraTS'20, D2: Kvasir-SEG, D3: DFU	\blacksquare D1: 85.5 \blacksquare D2: 88.1 \blacksquare D3: 75.7